

THESIS FOR THE DEGREE OF DOCTOR OF PHILOSOPHY IN NATURAL SCIENCE,
SPECIALISING IN CHEMISTRY

**A Soot Transformation Study:
Interactions Between Soot, Sulfuric Acid and
Secondary Organic Aerosol (SOA)**

Xiangyu Pei



UNIVERSITY OF GOTHENBURG

Department of Chemistry and Molecular Biology
University of Gothenburg
Gothenburg, Sweden

A Soot Transformation Study: Interactions Between Soot, Sulfuric Acid and
Secondary Organic Aerosol (SOA)

© Xiangyu Pei, 2018

Atmospheric Science,
Department of Chemistry and Molecular Biology,
University of Gothenburg,
SE-412 96 Gothenburg,
Sweden

Printed by BrandFactory AB
Källered, Sweden 2018

ISBN: 978-91-629-0306-0 (PRINT)

ISBN: 978-91-629-0307-7 (PDF)

<http://hdl.handle.net/2077/54249>

Cover picture: Soot transformation and its importance on the globe

Abstract

Atmospheric black carbon (BC), generally called soot, is the most important aerosol component that warms the Earth's climate significantly, and reducing atmospheric soot level has been proposed as a strategy for near-term climate change mitigation. However, policy development is hampered by large uncertainties in models' predictions regarding the global warming induced by BC. These uncertainties primarily result from a limited scientific understanding of the transformations soot undergoes upon interacting with other aerosol components such as sulfuric acid and secondary organic aerosol (SOA). Unlike soot, sulfuric acid and SOA are thought to induce cooling effects. However, soot – sulfuric acid – SOA interactions are postulated to amplify soot's warming effect. Condensed materials such as sulfuric acid and SOA can modify soot's morphology, i.e. the distribution of soot aggregates and condensates in space, thereby altering its properties and atmospheric life time. The overall aim of this thesis is to characterize freshly emitted soot and the transformations in morphology and optical properties it undergoes upon condensation of sulfuric acid and SOA.

Two frameworks were developed for quantifying the *in-situ* morphological properties of BC mixed with either primary organic aerosol (POA) during evaporation process or sulfuric acid and/or SOA during condensation process. The morphological transformation of soot particles was quantified with these frameworks in terms of void fractions, effective densities, and *in-situ* dynamic shape factors. Soot morphological transformation during condensation process was shown to occur via two complementary and sequential processes: the filling of voids within particles and mobility diameter growth.

In addition, the light absorption of soot from two flame types (an industrial flame and three lab-scale flames) was studied. Significant quantities of light absorbing organics (referred to as brown carbon, BrC) were observed in lab-scale flames, but the mature soot in the industrial flame did not contain BrC. The mass absorption cross section (MAC) of BC and BrC from lab-scale flames was quantified, and the values for BrC proved to be comparable to those for BC at a short wavelength (405 nm). The most widely used model for quantifying the optical properties of coated soot at present is core-shell Mie theory, in which the key parameter is the refractive index. This study identified and evaluated alternatives to Mie theory. It was found that the nature of the condensed material can significantly influence the light absorption of coated soot particles, and that reaction between soot and sulfuric acid can have particularly important effects. The absorption cross section of soot was significantly reduced (by up to 26%) upon interaction of the soot surface with sulfuric acid, whereas the absorption cross section increased significantly when soot was coated with SOA or acidity-mediated SOA.

Field studies of soot coated with other aerosol components, i.e. organics, sulfate and nitrate, were conducted in Beijing, and the results were compared to the lab studies. The findings suggested that ambient BC particles during summertime in Beijing was internally mixed and heavily coated since their effective density was similar to the material density of the coatings.

Keywords: soot, black carbon (BC), brown carbon (BrC), primary organic aerosol (POA), secondary organic aerosol (SOA), sulfuric acid, acidity-mediated SOA, mixing state, morphology, effective density, light absorption

Abstract (in Swedish)

Atmosfäriskt svart kol (BC), allmänt kallat sot, är den viktigaste aerosolkomponenten som signifikant värmer jordens klimat och en reduktion av koncentrationerna av sot i atmosfären har föreslagits som en strategi för kortsiktig klimatförändring. Policyutvecklingen för detta hindras emellertid av stora osäkerheter i klimatmodellerna angående hur stor del av den globala uppvärmningen som orsakas av BC. Dessa osäkerheter beror främst på en begränsad vetenskaplig förståelse för de transformationer som sot genomgår i samverkan med andra aerosolkomponenter, såsom svavelsyra och sekundära organiska aerosoler (SOA). Till skillnad från sot partiklar inducerar partiklar med enbart svavelsyra och SOA kylningseffekter på klimatet. Dock förmodas en blandad partikel där sot – svavelsyra – och SOA-interagerar att förstärka sotets uppvärmningseffekt. Det kondenserade material på sot, såsom svavelsyra och SOA, modifiera sotets morfologi, dvs dess struktur som i ren form ofta är oregelbunden, varigenom dess egenskaper och atmosfärisk livstid förändras. Det övergripande syftet med denna avhandling är att karakterisera nyemitterad sot och de omvandlingar sot genomgår vid kondensation av svavelsyra och SOA vilket påverkar dess morfologi och optiska egenskaper.

Två teoretiska ramverk utvecklades för att *in situ* kvantifiera de morfologiska egenskaperna hos BC blandad med antingen primär organisk aerosol (POA) under en avdunstningsprocess eller svavelsyra och/eller SOA under en kondensationsprocess. Den morfologiska omvandlingen av sotpartiklar kvantifierades med dessa ramverk i termer av hålrumsfraction, effektiv densitet och dynamisk figurfaktorer. Sots morfologiska omvandling under kondensation visade sig ske via två komplementära och sekventiella processer: fyllning av hålrum i sotaggregaten och tillväxt av mobilitetsdiametern.

Dessutom studerades ljusabsorptionen av sot från två typer av förbränningslägor (en industriell låga och tre lågor i laboratorieskala). Betydande mängder ljusabsorberande organiska ämnen (kallat brunt kol, BrC) observerades i lågor i laboratorieskala, medan sotaggregaten i den industriella lågan inte innehöll BrC. Massabsorptionstvärsnittet (MAC) av BC och BrC från lågor i laboratorieskala kvantifierades och värdena för BrC visade sig vara jämförbara med de för BC vid en kort våglängd (405 nm). Den mest använda modellen för att kvantifiera de optiska egenskaperna hos belagt sot är för närvarande Mie-teori, där nyckelparametern är brytningsindex. Denna studie identifierade och utvärderade alternativ till Mie-teorin. Man fann att det kondenserade materialet signifikant kan påverka absorptionen hos belagda sotpartiklar och att reaktionen mellan sot och svavelsyra kan ha särskilt viktiga effekter. Absorptionstvärsnittet av sot minskade signifikant (med upp till 26%) vid interaktion av sotytan med svavelsyra, medan absorptionstvärsnittet ökade signifikant när sot täcktes med SOA.

Fältstudier av sot belagt med andra aerosolkomponenter, dvs organiska ämnen, sulfat och nitrat, genomfördes i Peking, och resultaten jämfördes med laboratoriestudierna. Resultaten visar att under sommarperioden i Peking var omgivande BC-partiklar internt blandade och belagda med mycket kondensat eftersom deras effektiva densitet var nära densitet av det kondenserade materialet.

List of publications

Publications included in this thesis work

Paper I: Measurement of the size distribution, volume fraction and optical properties of soot in an 80 kW propane flame

D. Bäckström, A. Gunnarsson, D. Gall, X.Y. Pei, R. Johansson, K. Andersson, R. K. Pathak, J. B. C. Pettersson

Combust. Flame, 2017, 186, 325-334.

Paper II: Morphological and optical characteristics of atmospherically relevant black and brown carbon formed in propane fueled flames

X.Y. Pei, M. Hallquist, E. Ljungström, S. Guo, J. H. Pagels, N. M. Donahue, B. Svenningsson, A. C. Eriksson, R. K. Pathak

Manuscript in preparation for Aerosol Sci. Technol.

Paper III: Morphological transformation of soot: investigation of microphysical processes during the condensation of sulfuric acid and limonene ozonolysis product vapors

X.Y. Pei, M. Hallquist, A. C. Eriksson, J. H. Pagels, N. M. Donahue, T. Mentel, B. Svenningsson, W. Brune, R. K. Pathak

Atmos. Chem. Phys. Discuss., 2017, <https://doi.org/10.5194/acp-2017-769>.

Paper IV: Changes in soot optical properties via interactions with sulfuric acid and limonene ozonolysis products coatings

X.Y. Pei, M. Hallquist, R. K. Pathak

Manuscript in preparation.

Paper V: Size-resolved effective density of submicron particles during summertime in the rural atmosphere of Beijing, China

K. Qiao, Z.J. Wu, X.Y. Pei, Q.Y. Liu, D.J. Shang, J. Zheng, Z.F. Du, Y.S. Wu, S. Guo, C. K. Chan, R. K. Pathak, M. Hallquist, M. Hu

J. Environ. Sci., *accepted after minor revision.*

Software associated with Paper V: Control software for continuous measurement system of Centrifugal Particle Mass Analyzer (CPMA)

Copyright Holder: X.Y. Pei

Computer Software Copyright Registration Certificate No. 2044928, National Copyright Administration, P. R. China.

Author's contribution to the papers and the manuscripts

Paper I: The author operated the PASS-3 instrument during the measurements and participated in the data analysis, discussion, and evaluation of results.

Paper II: The author participated in the planning of the study, conducted the measurements, performed the data analysis, and wrote the paper in collaboration with the co-authors.

Paper III: The author participated in the planning of the study, conducted the measurements, performed the data analysis, and wrote most of the paper in collaboration with the co-authors.

Paper IV: The work presented in this paper was part of the study first reported in Paper III, so the author's contributions are as indicated above.

Paper V: The author helped design the measurement strategy, wrote the control software, and operated the CPMA instrument during the measurement campaign. The author also participated in the data analysis, discussion, and evaluation of results.

Other publications (not included in this thesis)

1. Characteristics of regional new particle formation in urban and regional background environments in the North China Plain
Z.B. Wang, M. Hu, J.Y. Sun, Z.J. Wu, D.L. Yue, X.J. Shen, Y.M. Zhang, **X.Y. Pei**, Y.F. Cheng, and A. Wiedensohler
Atmos. Chem. Phys., 2013, 13, 12495-12506.
2. Connection of organics to atmospheric new particle formation and growth at an urban site of Beijing
Z.B. Wang, M. Hu, **X.Y. Pei**, R.Y. Zhang, P. Paasonen, J. Zheng, D.L. Yue, Z.J. Wu, M. Boy, A. Wiedensohler
Atmos. Environ., 2015, 103, 7-17.
3. Impact of the 0.1% fuel sulfur content limit in SECA on particle and gaseous emissions – Case of low-sulfur residual marine fuel oil
M. Zetterdahl, J. Moldanová, **X.Y. Pei**, R. K. Pathak, B. Demirdjian
Atmos. Environ., 2016, 145, 338-345.
4. Contribution of volatile and non-volatile compounds (at 300°C) to condensational growth of atmospheric nanoparticles: an assessment based on 9-years observations at the Central Europe background site Melpitz
Z.B. Wang, W. Birmili, A. Hamed, B. Wehner, G. Spindler, **X.Y. Pei**, Z.J. Wu, Y.F. Cheng, H. Su, A. Wiedensohler
J. Geophys. Res.: Atmos., 2017, 122, 485-497.
5. Ice nucleating particle concentrations unaffected by urban air pollution in Beijing, China
J. Chen, Z.J. Wu, S. Augustin-Bauditz, S. Grawe, M. Hartmann, **X.Y. Pei**, Z.R. Liu, D.S. Ji, H. Wex
Atmos. Chem. Phys. Discuss., 2017, <https://doi.org/10.5194/acp-2017-884>.
6. On-road assessment of city buses in Gothenburg: Gaseous and particle emission factors of regulated pollutants
Q.Y. Liu, Å. M. Hallquist, M. Le Breton, **X.Y. Pei**, M. Hallquist, R. K. Pathak, T.Y. Liu, C. K. Chan
Manuscript in preparation for Environ. Sci. Technol.

Table of Contents

Abstract	i
Abstract (in Swedish)	ii
List of publications	iii
Table of Contents	vii
List of Abbreviations	ix
Chapter I	
Introduction	1
Chapter II	
Background	3
2.1 Combustion aerosols	3
2.2 Properties of fresh soot	4
2.3 Atmospheric aging of soot	5
2.4 Effects on climate and health	7
Chapter III	
Experimental methods	9
3.1 Characterization of industrial in-flame soot	9
3.1.1 Experimental facility	9
3.1.2 Measurement system	10
3.2 Characterization of lab-scale flame soot	10
3.2.1 Soot generator	10
3.2.2 Experimental setup	11
3.3 Setup for studying soot transformation	13
3.3.1 Soot generation	13
3.3.2 Soot modification	13
3.4 Instrumentation	14
3.4.1 Size-resolved particle mass measurement with DMA-APM/CPMA	14
3.4.2 Absorption measurement with a PASS-3	15
3.4.3 Size distribution measurement with a SMPS	16
3.4.4 Radiative intensity measurement with a narrow angle radiometer	16
3.5 Data analysis	16
3.5.1 Particle morphology	16
3.5.2 Optical properties	18
Chapter IV	
Results and discussion	21
4.1 Characteristics of industrial in-flame soot	21
4.2 Characteristics of lab-scale flame soot	24
4.2.1 Composition and mixing state of soot	24
4.2.2 Morphology of soot	26
4.2.3 Absorption properties of BC and POA	29
4.3 Morphological transformation of soot	30
4.3.1 Framework to quantify the morphology	30

4.3.2	Particle void-filling and diameter growth.....	31
4.3.3	Dynamic shape factor	33
4.4	Changes in optical properties of soot.....	34
4.4.1	Effects of sulfuric acid condensation on BC.....	34
4.4.2	Lensing effect and the role of condensed material.....	36
4.4.3	Framework to quantify the changes in optical properties	37
4.5	Effective densities of ambient particles during field measurements.....	39
Chapter V		
Conclusions		43
Acknowledgements.....		45
References.....		47

List of Abbreviations

AAE	<i>Ångström Absorption Exponent</i>
APM	<i>Aerosol Particle Mass Analyzer</i>
BC	<i>Black Carbon</i>
BrC	<i>Brown Carbon</i>
C_{abs}	<i>Absorption Cross Section</i>
CCN	<i>Cloud Condensation Nuclei</i>
COPD	<i>Chronic Obstructive Pulmonary Disease</i>
CPC	<i>Condensation Particle Counter</i>
D_{fm}	<i>Mass Mobility Exponent</i>
DMA	<i>Differential Mobility Analyzer</i>
D_{me}	<i>Mass Equivalent Diameter</i>
D_p	<i>Particle Mobility Diameter</i>
d_{pp}	<i>Primary Particle (Spherules) Diameter</i>
E_{abs}	<i>Absorption Enhancement</i>
G_{fd}	<i>Particle Diameter Growth Factor</i>
k_{POA}	<i>Imaginary Refractive Index of POA</i>
MAC	<i>Mass Absorption Cross Section</i>
MFC	<i>Mass Flow Controller</i>
m_p	<i>Particle Mass</i>
NOC	<i>Nanoscale Organic Carbon</i>
OA	<i>Organic Aerosol</i>
PAHs	<i>Polycyclic Aromatic Hydrocarbons</i>
PASS-3	<i>Photo Acoustic Soot Spectrometer at 3 Wavelengths</i>
PM	<i>Particulate Matter</i>
POA	<i>Primary Organic Aerosol</i>
RI	<i>Refractive Index</i>
SMPS	<i>Scanning Mobility Particle Sizer</i>
SOA	<i>Secondary Organic Aerosol</i>
SSA	<i>Single Scattering Albedo</i>
TD	<i>Thermo-Denuder</i>
VOCs	<i>Volatile Organic Compounds</i>

VTDMA	<i>Volatility Tandem Differential Mobility Analyzer</i>
χ	<i>Dynamic Shape Factor</i>
Δr_{me}	<i>Mass Equivalent Coating Thickness</i>
ρ_{eff}	<i>Effective Density</i>
ρ_m	<i>Material Density</i>
Φ	<i>Fuel-Air Equivalence Ratio</i>

Chapter I

Introduction

Current air quality and climate models cannot accurately describe the influence of short-lived climate forcers such as O_3 , CH_4 , and aerosols. For aerosols, uncertainties exist because their formation, and transformation in the atmosphere are complex processes that strongly affect their composition and hence their properties. For instance, one common aerosol component, soot, is believed to have a warming effect, whereas secondary organic aerosol (SOA) is thought to cool the planet¹. Even greater uncertainties are associated with aerosols' indirect climate effects, such as their influence on cloud properties. Of the major components included in current models, SOA is arguably the least well-described; there are large discrepancies between experimental observations and models' predictions of its behavior²⁻⁴. In addition, sulfuric acid – ubiquitous in the atmosphere – can condense on soot, changing its properties and providing active acidic surfaces for the condensation of semi-volatile SOA. As a result, the influence of soot – SOA interactions mediated by sulfuric acid must be well understood, characterized, and parameterized to clarify their effects on climate and facilitate more accurate climate modeling.

In this thesis, I try to improve the fundamental understanding of the physical properties of freshly emitted soot and soot during transformation, including its mixing state, morphology and optical properties. The thesis is a comprehensive summary of various articles that have been published or are in the process of publication.

Paper I: The size distribution, volume fraction, absorption and scattering coefficients of soot in an 80 kW swirling propane-fired flame were measured. The radiative emissions of the flame's gases and particles were estimated using a statistical narrow-band model and Rayleigh theory, respectively, and compared to the measured total radiative intensity.

Paper II: The mixing of black carbon (BC) with primary organic aerosol (POA), and the resulting morphological transformation, were studied experimentally. A new framework for quantifying the *in-situ* morphological properties of BC mixed with POA (subsequently referred to as brown carbon, BrC) was developed using mass and mobility measurements of particles from laboratory propane flames. Additionally, the optical characteristics, i.e. the mass absorption cross section (MAC), of POA and BC were quantified and compared.

Paper III: The influence of condensation of vapors of sulfuric acid, and/or limonene ozonolysis products on the morphological transformation of soot aggregates was investigated systematically. A framework for quantifying the microphysical transformation of soot upon the condensation of various materials was developed and used to interpret the *in-situ* morphological state of the soot in terms of the fractions of internal/open voids filled, surface growth, and a dynamic shape factor.

Paper IV: The changes in optical properties of soot upon the condensation of pure sulfuric acid, limonene ozonolysis SOA, and acidity-mediated limonene SOA were systematically investigated. The absorption cross section of uncoated and coated soot particles was measured and compared to the predictions of core-shell Mie theory. A framework describing the changes in optical properties of soot was developed to quantify the major processes during condensation of coating materials, and mechanisms for these processes were proposed to explain the differences between the measurements and the predictions of Mie theory.

Paper V: The size-resolved effective density of 50–350 nm particles was determined at a rural site in Beijing (the Changping site) during an intensive field campaign conducted in the summer of 2016 to study the mixing state and morphology of atmospheric aerosols.

Studies on fresh soot are reported in Papers I and II: Paper I presents a characterization of soot from large flames in an industrial facility, while Paper II characterizes soot from lab-scale flames. These studies showed that soot in industrial flames has similar light-absorbing characteristics to that in laboratory flames, i.e. both flame types have a similar Ångström absorption exponent (AAE). Such laboratory flames may therefore be good models of real industrial soot-forming flames. Papers III and IV describe the morphological transformation and changes in optical properties of such lab flame soot particles following the condensation of sulfuric acid and/or organic aerosols, and together provide a holistic picture of soot transformations in the atmosphere. The effective density of real atmospheric soot particles coated with other aerosol components such as SOA, sulfate and nitrate was quantified using mass-mobility measurements in Paper V, revealing that heavily coated soot particles underwent far more pronounced transformations than had been observed in the laboratory studies reported in Papers II and III.

Chapter II

Background

2.1 Combustion aerosols

Combustion generates aerosol particles consisting of black carbon (BC, also known as soot) and primary organic aerosol (POA), which are the major constituents of anthropogenic ambient particulate matter (PM)⁵. These particles can affect human health adversely⁶ and act as strong climate forcers¹. Whereas particles of other substances such as secondary organic aerosol (SOA), sulfate, and nitrate induce light scattering and thus have a cooling effect on the climate, soot is the second most important anthropogenic pollutant after carbon dioxide in terms of its warming effect because of its strong light absorption⁷. Its formation is accompanied by that of other primary gases and aerosol components, and it is generally not well characterized. Despite being a primary pollutant from combustion processes, it undergoes atmospheric transformations due to its interactions with other gases and aerosol components such as organic aerosol (OA), leading to changes in its initial properties⁸. The other key component formed in combustion processes is POA, which can also contribute to light absorption, especially in the ultra-violet (UV)-to-visible-light wavelength range. These substances are collectively referred to as primary or secondary brown carbon (BrC), depending on whether they are formed by primary or secondary processes^{9,10}.

Polycyclic aromatic hydrocarbons (PAHs) are believed to be the molecular precursors of soot particles¹¹ in flames. Soot formation starts with inception, i.e. the initial appearance of PAH clusters. These clusters nucleate and grow to form nanoscale organic carbon (NOC) particles¹². The nucleated NOC particles, also known as nascent soot particles, then grow to larger size via surface growth resulting from surface chemical reactions (hydrogen-abstraction carbon-addition, HACA)¹³ and surface adsorption of PAHs, and also through particle coagulation and coalescence. Nascent soot particles lose hydrogen and become more carbonized and graphitic when they spend more time in high temperature zones of the flame¹⁴. Carbonized soot particles, known as mature soot, are formed by the aggregation of solid spherical primary particles (spherules), after which co-produced POA condenses on the soot surface¹⁵. Finally, soot particles can lose mass and size via oxidation and fragmentation processes. Flame-generated mature soot contains many clusters of sp^2 -hybridized carbons⁸ whose π electrons move freely and have closely spaced energy levels, allowing them to absorb electromagnetic radiation over a wide wavelength range. Mature soot also contains sp^3 -hybridized carbons, which surround the sp^2 clusters⁸. Figure 2.1 depicts the key processes of soot formation.

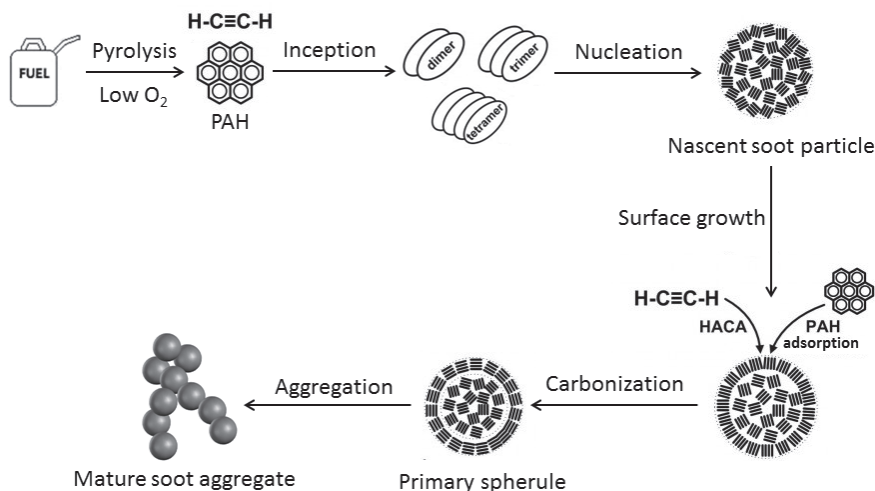


Figure 2.1 Key soot formation processes (modified from Kholghy et al.¹⁵).

2.2 Properties of fresh soot

The morphological structure of soot aggregates can be described in terms of the mass-mobility exponent (Dfm)¹⁶. The tandem differential mobility analyzer (TDMA) technique has been widely used to characterize the volatile and non-volatile mass fractions of BC-POA mixtures, and the morphology of fresh soot. The Dfm of fresh diesel soot is typically in the range of 2.2–2.4^{17,18}, indicating a relatively chain-like open structure (spherical particles have a Dfm of 3.0).

BC is the most efficient light-absorbing aerosol in the atmosphere; its mass absorption cross section (MAC) is commonly taken to be $7.5 \pm 1.2 \text{ m}^2 \text{ g}^{-1}$ at a wavelength of 550 nm⁸. The Ångström absorption exponent (AAE, a measure of the wavelength dependence of light absorption) for BC is typically assumed to be ~ 1.9 ,¹⁹ and a wavelength-independent refractive index (RI) of $1.95 - 0.79i$ is recommended⁸, although it may actually have a very weak wavelength dependence²⁰. The MAC of BrC is much more strongly wavelength-dependent – its AAE value ranges from 2–6²¹ – so the imaginary part of the RI for BrC is also strongly wavelength dependent²². The difference in the AAE values for BC and BrC indicates that BC absorbs light over the full visible spectrum, but BrC absorbs more light at shorter wavelengths than at longer ones. BrC is believed to account for 20–50% of the total light absorption by atmospheric particles in the UV wavelength range²³, so it significantly affects the atmosphere's radiative balance and photochemistry. Fresh soot is hydrophobic or limited in hygroscopicity, but it may become hydrophilic after atmospheric transformation^{24,25}.

2.3 Atmospheric aging of soot

Fresh soot undergoes transformations including various atmospheric mixing and aging processes after being emitted from combustion sources. Mixing with other types of aerosol and aging by condensation of secondary species such as SOA, sulfate, and nitrate can alter the morphology of soot aggregates by collapsing them into more compact shapes^{26,27} in a process known as restructuring. Aging can also significantly change soot's optical properties²⁸⁻³⁰, for instance by enhancing its absorption and scattering capabilities, and by making initially hydrophobic soot particles more hydrophilic, thereby enhancing their ability to act as cloud condensation nuclei (CCN)^{25,31-33}. Figure 2.2 depicts soot aging processes and the associated morphological, optical, and hygroscopicity changes.

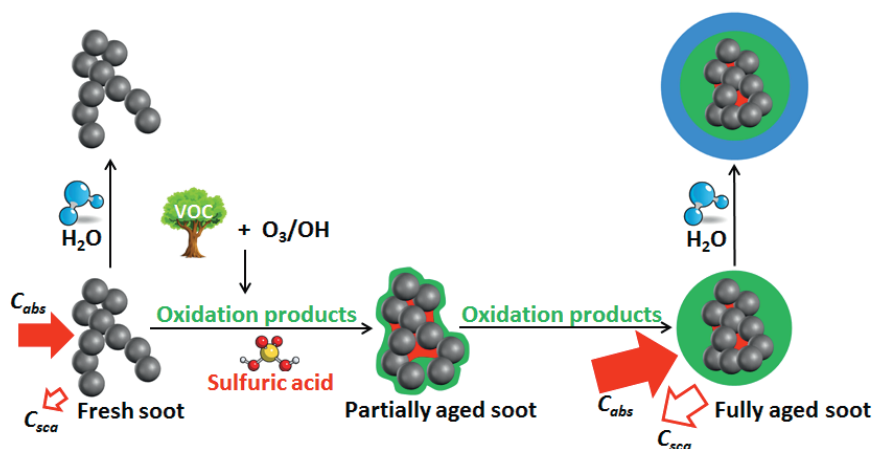


Figure 2.2 Selected soot aging processes and the associated changes in morphological, optical, and hygroscopic properties.

Previous studies^{25,34} have shown that under water saturation (relative humidity, RH < 100%), fresh hydrophobic soot exhibited only a relatively small amount of hygroscopic growth, indicating that water vapor had little effect on the morphology of soot in the sub-saturation state. However, if water-soluble compounds such as sulfuric acid or organic matter condensed on their surfaces, soot particles became hydrophilic, potentially causing morphological transformation of the soot core that gave rise to a more spherical shape as the RH increased^{25,26}; this was reflected in an increased D_{fm} . The degree of collapse depended on the combustion conditions during soot generation, and also the type and mass fraction of the coating material. Soot aggregates generated by spark discharge can collapse into relative compact shapes, but diesel soot was relatively resistant to collapse²⁴. Different dicarboxylic acids had different effects on soot collapse. Exposure to glutaric acid (C₅, low RH_{deliquescence}) caused significant collapse of the soot core, but condensation of succinic

acid (C_4 , high $RH_{deliquescence}$) had no effect on soot morphology³⁵. SOA formed by OH-initiated oxidation of toluene and isoprene also caused collapse of soot cores^{31,33}.

The MAC of freshly emitted soot may be reduced as the soot aggregates collapse into more compact shapes due to “shielding effect” whereby the outer primary spherules of the collapsed soot core block interactions between inner primary spherules and incident light³⁶. Interactions between adjacent primary spherules are believed to increase the MAC of soot aggregates by up to 30% relative to the sum of the MAC values of the isolated primary spherules in the soot. This enhancement can be suppressed by common coatings such as organics and sulfate, which are dielectric materials and thus reduce the electromagnetic coupling between the primary spherules even when the soot particles are only covered with thin coatings³⁷. In laboratory experiments, the absorption enhancement of coated soot under controlled conditions varied markedly (from 1.05 to 3.50 relative to fresh soot) with changes in the size and morphology of the soot cores and the types and quantities of coatings^{30,38-40}. However, no obvious absorption enhancement was observed in laboratory experiments where soot was coated with OH-initiated oxidation products of toluene and m-xylene^{31,41}. Field measurements yielded absorption enhancements of 1.2 to 1.6 in the vicinity of the source region^{42,43}. An absorption enhancement of 1.4 induced by ambient aerosols was observed in the UK⁴⁴, and strong absorption enhancements of 2–3 were observed in Northern China when sulfate abundance increased rapidly⁴⁵. In contrast, negligible absorption enhancement (6%) was observed in the centers of large cities in North America, although the MAC values of the aged particles were 20–40% higher than that for fresh soot⁴⁶. Minimal absorption enhancement due to lensing effects was also observed in downtown Toronto, even under the influence of long-range transport events⁴⁷. Peng et al. reported that soot aging occurred in two distinct phases: an initial transformation from fractal aggregates to compact particles with little absorption enhancement, and the subsequent growth of fully compacted particles causing greater absorption enhancements of up to 2.5⁴⁸. This provided a potential explanation for the discrepancy between laboratory observations and field measurements. In addition to coatings under dry or low RH conditions, water is an important component of atmospheric aerosols. Particles can absorb moisture and grow to large sizes at high humidity or in clouds. However, it is difficult to measure the absorption enhancement under such conditions⁴⁹.

Fresh soot particles are hydrophobic and cannot function as CCN^{24,50}. Under ambient conditions, soot aggregates become hydrophilic via the condensation of hygroscopic organics or inorganics⁵¹ and grow by coagulation. They may acquire different kinds of coatings, including POA, SOA, or inorganics; specific examples include α -pinene ozonolysis products²⁴, adipic acid⁵², succinic or sulfuric acid⁵³, toluene OH oxidation products³¹, isoprene OH oxidation products³³, and toluene and m-xylene oxidation products under UV exposure⁵⁴.

2.4 Effects on climate and health

Soot can significantly influence the climate and human health after being emitted into the atmosphere. It affects the climate system via three main processes⁷: (i) absorption of solar radiation in the atmosphere, (ii) deposition onto snow and ice surfaces, and (iii) interactions with clouds affecting cloud albedo and lifetime.

Soot can strongly absorb solar radiation in the atmosphere, reducing the amount of sunlight reflected back to space and thereby reducing the planetary albedo. In addition, light absorption by soot warms the surrounding air and thus exerts a warming effect on the atmosphere, which is termed as direct effect¹. POA from fossil fuel and biomass/biofuel combustion processes also contributes substantially to light absorption and perturbs the atmosphere's radiative balance, causing a climatic warming effect²².

When soot is deposited on snow or ice, it darkens the material's white surface, reducing its albedo and warming it. As the temperature increases, more snow/ice melts, leaving a dark underlying surface of water and/or soil that further enhances the absorption of solar radiation. This process reduces the Earth's reflectivity and also causes climatic warming¹.

Interactions of soot with clouds produce semi-direct and indirect effects. The semi-direct effect is related to changes in the vertical temperature structure of the atmosphere due to local heating by soot^{7,55}. Atmospheric stability, convection and cloudiness can be affected by such perturbations of the temperature structure. The magnitude of the perturbation depends on the altitude of the emitted soot and the vertical soot distribution⁵⁵⁻⁵⁷. The indirect effect is related to the ability of soot or soot-containing particles to act as CCN and form cloud droplets by taking up water in the atmosphere, affecting cloud albedo and lifetime.

Combustion generated particles are expected to be more harmful to human health than non-combustion related particles⁵⁸. Particle exposure can cause irritation of the eyes, nose, and throat⁵⁹. The small size of soot particles (typical diesel soot particle size: ~70 nm) enables them to penetrate through the respiratory system and deposit in the bronchial and alveolar regions, increasing the risk of respiratory diseases such as asthma, chronic obstructive pulmonary disease (COPD) and lung cancer, and causing blood clotting and cardiovascular diseases via transportation into the blood⁶⁰. When hydrophilic materials condense on soot, the resulting increased hygroscopicity and compaction of the soot core enhance soot deposition in the lungs and bronchial airways, exacerbating these adverse effects⁶¹.

Chapter III

Experimental methods

Powerful experimental techniques are needed to understand soot formation and transformation processes. This section briefly introduces the experimental methods used to study different properties of soot.

3.1 Characterization of industrial in-flame soot

3.1.1 Experimental facility

Experiments designed to characterize soot in industrial flames were performed in the Chalmers 100 kW_{th} oxy-fuel test rig⁶², which is depicted in schematic form in Figure 3.1. The rig can be operated in air- or oxy-fired mode and allows recycling of flue gases. During experiments, it was exclusively fueled with propane, although it is compatible with both solid and gaseous fuels. The thermal input was 80 kW in all cases, and only air-fired conditions were studied. The height of the cylindrical combustion chamber is 240 cm and its inner diameter is 80 cm. There are measurement ports along the height of the combustion chamber; in this work, measurements were acquired through ports M2–M5. The burner has two annular swirling air registers: the primary air register and secondary air register. Two flame conditions were tested: Flame A was a flame with little soot, formed using the standard settings for the air split between the primary and secondary air, while Flame B had more soot (i.e. it was fuel-rich) and was formed by closing the primary air register.

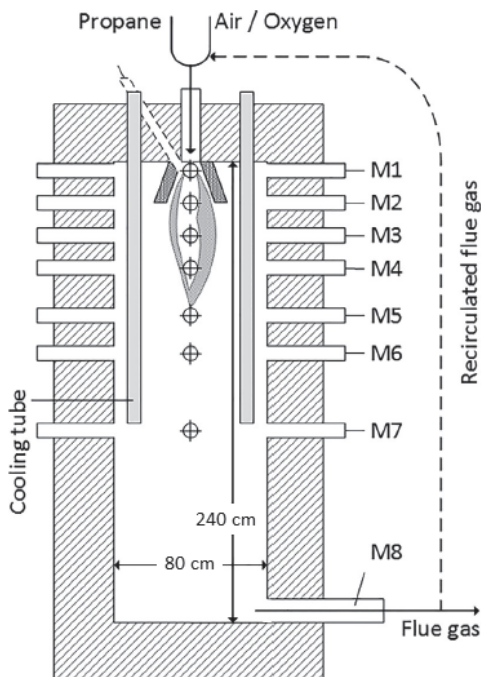


Figure 3.1 Schematic of the oxy-fuel test rig. Measurements were acquired via ports M2–M5.

3.1.2 Measurement system

A ~2 m long oil-cooled probe with an outer diameter of 30 mm was designed for the measurements. Using oil as the coolant allowed the probe to maintain a relatively high interior temperature, reducing the problem of in-probe condensation. The sample gas was diluted with nitrogen to cool it and quench reactions. A SMPS system was used to measure particle number size distributions, a PASS-3 instrument was used to measure the light absorption and scattering coefficients of soot particles, and a narrow angle radiometer was used to measure the flames' radiative intensity. Detailed descriptions of these instruments are presented in section 3.4.

3.2 Characterization of lab-scale flame soot

3.2.1 Soot generator

To perform controlled experiments in the laboratory, a soot generator was designed and built to generate submicron soot particles with adjustable (albeit interdependent) particle size distributions, BC fractions, and mixing states with organics. This generator was used in the studies reported in Papers II-IV. Unlike the widely used miniature combustion aerosols standard generator (mini-CAST, Jing Ltd.), which

produces soot in an N_2 -quenched laminar diffusion flame⁶³, the soot generator used in this work employs a combination of premixing and diffusion of air in a propane fueled, air-quenched flame, as shown in Figure 3.2. Premixing is achieved by controlled mixing of the flows of fuel and air before ignition. The dimensions of the tube delivering the fuel/air mixture to the flame zone are such that a flame travelling backwards in the system is quenched. Diffusion air is added through a tube with a larger diameter that is concentric with the fuel mixture tube. The system also offers the ability to "chop" the flame with a horizontal sheet of air that quenches the combustion. Dilution air can be added to reduce particle concentrations if desired. The premixing, diffusion, quenching and dilution air were generated with a commercially available system (GC 15000, SCHMIDLIN Labor & Service AG). The fuel and air mass flows were regulated by mass flow controllers (MFC). Different flame conditions were realized by changing the flow rate of each gas line and thus the Fuel-Air Equivalence Ratio (Φ). The soot generator was maintained at slightly above atmospheric pressure by the pressure drop over the transfer line to the measurement equipment and excess vent.

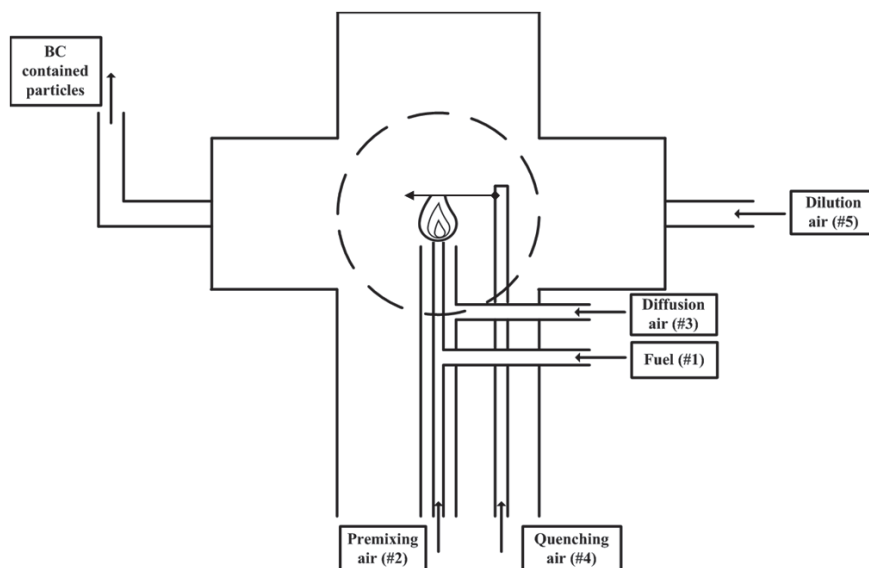


Figure 3.2 Design of the new soot generator that combines premixed and diffusion combustion.

3.2.2 Experimental setup

The experimental setup used to characterize lab-scale flame soot in Paper II is shown in Figure 3.3. The aerosol from the soot generator was dried in a silica gel diffusion dryer prior to further modification. A differential mobility analyzer (DMA1, model 3081, TSI Inc., aerosol flow rate 0.4 l min^{-1} , and sheath flow rate 3.0 l min^{-1}) preceded

by a bipolar neutralizer (^{63}Ni) was used to enable size-selection of the dried aerosol to produce monodisperse particle. To study polydisperse aerosols, the DMA1 was bypassed. A thermo-denuder (TD) was introduced to remove the primary organic coating on soot particles⁶⁴. The TD was maintained at 400 °C with a residence time of ~20 s. Under these conditions, monodisperse particles in the size range 50–400 nm exhibited a 17% loss in number concentration on average. This loss rate was used to correct the number concentration due to diffusion and thermophoresis. Mixtures of pure BC and OC were obtained when no thermo-denuder (NTD) was used, but pure BC particles were obtained when soot was passed through the TD. After the TD, the samples were passed through charcoal granules (Activated Charcoal Powder USP, Spectrum Chemical Mfg. Corp.) in a NO_x denuder to remove NO_x . The mixing state of the soot aerosol was characterized using a volatility tandem DMA (VTDMA) system⁶⁵ consisting of two DMAs (DMA1 and DMA2), a condensation particle counter (CPC), and a thermo-denuder (TD) arranged as shown in Figure 3.3. The OC and BC mass fractions were determined using the VTDMA system and an aerosol particle mass analyzer (APM). Optical properties including absorption coefficients were measured using a photo-acoustic soot spectrometer operating at three wavelengths (PASS-3), namely 405, 532 and 781 nm. Detailed descriptions of these instruments can be found in section 3.4. Three flames (Exp. F1, Exp. F2 and Exp. F3) were examined in the experiments (see Paper II for the corresponding settings).

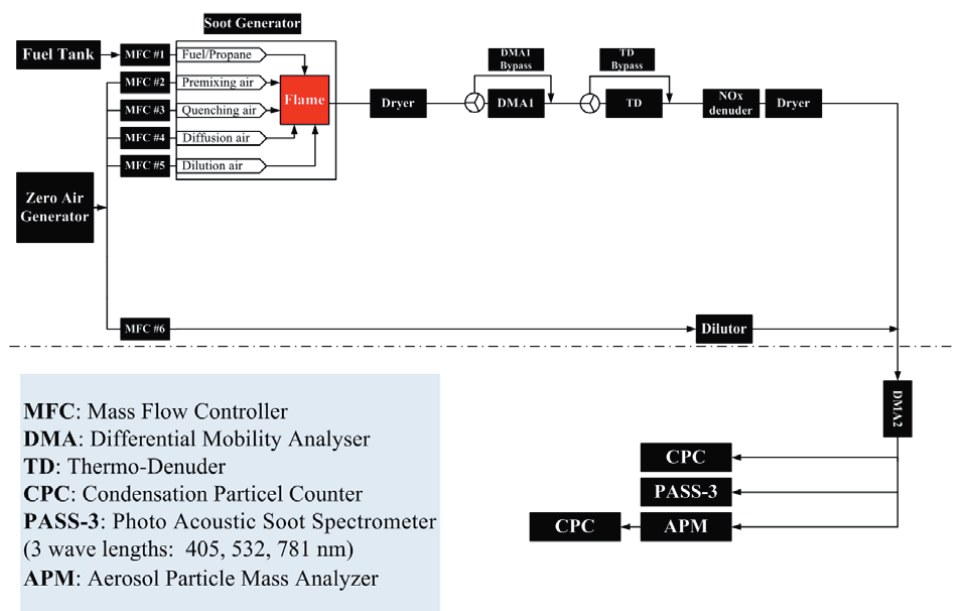


Figure 3.3 Schematic of the experimental setup for characterizing soot from lab-scale flames.

3.3 Setup for studying soot transformation

3.3.1 Soot generation

The soot from the soot generator was dried with a silica gel diffusion drier and then passed through a TD to remove co-produced primary organic components, as shown in Figure 3.4. The TD was maintained at 400 °C and the particle residence time within the TD was ~1.6 min. Downstream of the TD, a NO_x denuder filled with charcoal granite (Activated Charcoal Powder USP, Spectrum Chemical Mfg. Corp.) was used to remove NO_x. The polydisperse pure BC particles emerging from the denuder were neutralized with a bipolar neutralizer (⁶³Ni) and then selected using the first DMA (DMA1, model 3081, TSI Inc., aerosol flow rate 0.4 l min⁻¹, sheath flow rate 6.0 l min⁻¹) to obtain size-resolved particles for modification and characterization.

3.3.2 Soot modification

Soot particles were modified using the tandem DMA (TDMA) experimental setup with the integrated flow-tube system and then characterized using the APM, DMAs, and CPC as shown in Figure 3.4. Size-selected monodisperse soot cores were modified with sulfuric acid in a cylindrical glass mixing chamber (47 cm long and 10 cm in diameter) equipped with a temperature-controlled bath system. The modified soot particles were then further modified with SOA generated by limonene ozonolysis in a dark low-NO_x laminar flow tube with a flow rate of 1.52 l min⁻¹, an effective particle residence time of 4.8 min at 25 °C, and regulated RH (5±1%).

Soot cores of four nominal sizes (75, 100, 150, and 200 nm) were selected using DMA1. The experimental matrix included four major procedural steps: (i) characterization of the pure soot cores; (ii) modification of soot cores with sulfuric acid and subsequent characterization; (iii) modification of soot cores with SOA and subsequent characterization; and (iv) modification of the sulfuric acid modified soot with limonene ozonolysis products (acidity-mediated SOA) and subsequent characterization.

Soot samples were modified with sulfuric acid using a temperature-regulated bath system at three different temperatures: 1 °C (small = S), 5 °C (medium = M) or 25 °C (large = L). In the SOA modification steps, the limonene concentration in the flow tube was regulated by flowing zero air (Ultra Zero Air Generator GT 3000, LNI SCHMIDLIN AG) over limonene in a diffusion vial submersed in a temperature regulated bath system⁶⁶. The limonene mixing ratios in the flow-tube (56 ppb, 73 ppb, 138 ppb) were precisely regulated by setting the temperatures of limonene vial bath system to 1 °C (small = S), 5 °C (medium = M), or 15 °C (large = L) at a constant zero air flow rate (0.002 l min⁻¹). Ozone was generated by passing zero air through a UV-lamp unit (SOG-3, UVP). The ozone concentration for experiments was set to a

constant value of $1400 \mu\text{g m}^{-3}$ (~ 730 ppb) and monitored using a UV photometric ozone analyzer (model 49C, Thermo Environmental Instruments Inc.).

In all experiments involving pure soot core characterization, all modification steps involving sulfuric acid and limonene SOA were bypassed. When studying the effect of sulfuric acid modification alone on the morphological and optical properties of soot, only modification step involving limonene SOA were bypassed (by turning off the UV-lamp's power supply and thereby disabling ozone production). When studying the effects of SOA alone, modification step involving sulfuric acid were bypassed.

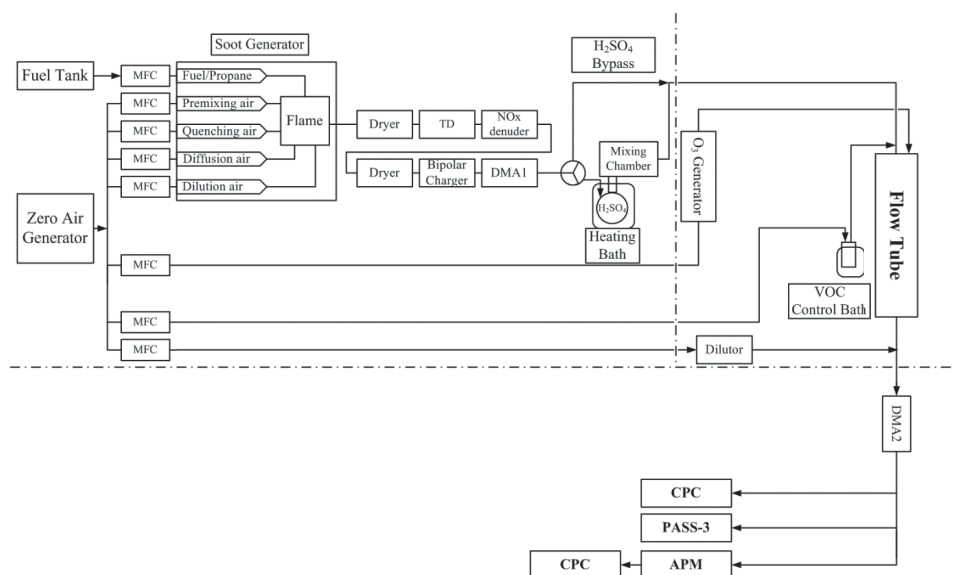


Figure 3.4 Schematic of the experimental setup for the soot transformation study.

3.4 Instrumentation

This subsection describes the key components of the setups and apparatus used for field measurements and for characterizing industrial in-flame soot, lab-scale flame soot, and soot transformation.

3.4.1 Size-resolved particle mass measurement with DMA-APM/CPMA

In Papers II–IV, the mass of monodisperse particle population after DMA2 was measured using an APM (model APM-3600, Kanomax) and a CPC (model 3775, TSI Inc., flow rate 0.3 l min^{-1}) connected in series. The APM consists of two concentric cylinders rotating at the same angular speed. A voltage is applied over the cylinders,

and particles introduced into the gap between the cylinders experience a centrifugal force. Only particles whose mass to charge ratio is such that the electric force equals the centrifugal force are transmitted through the APM and counted by the CPC⁶⁷. As the radius increases, the centrifugal force also increases but the electrical force decreases. Therefore, the forces are only balanced at one radial point, and only particles that travel along a path entering at this position will be correctly classified. Particles entering at other radial positions, even if they have the desired mass to charge ratio, may be lost to the cylinders, reducing particle transmission. Moreover, for the same reason, some particles with the wrong mass to charge ratio could be transmitted, thus broadening the instrument's response⁶⁸. During the experiments, the DMA-APM system was calibrated using two sizes of polystyrene latex spheres (Duke Scientific Corp.), as described previously⁶⁹. Since the APM actually classifies particles based on their mass to charge ratio, the presence of multiply charged particles could cause overestimation of the mass of the total particle population. The sensitivity of mass measurements to multiply charged particles was tested, revealing that it overestimated sample masses by less than 5% for all sizes of soot particles.

In Paper V, a centrifugal particle mass analyzer (CPMA, Cambustion Limited Co.) using the same operating principles as the APM was used to measure particle masses at a rural site in Beijing during summertime. Unlike the APM, the inner cylinder of the CPMA⁷⁰ rotates slightly faster than the outer cylinder to offset the decrease in centrifugal force towards the inner cylinder. This allows the forces to be balanced all the way across the classification zone. The DMA (model 3081, TSI Inc.) and CPC (model 3772, TSI Inc.) were used during this measurement campaign.

3.4.2 Absorption measurement with a PASS-3

In Papers I, II, and IV, a PASS-3 instrument (Droplet Measurement Technologies)⁷¹ was used to measure particles' in-situ light absorption coefficients simultaneously at wavelengths of 405, 532, and 781 nm with a time resolution of 2 s. Sample air was drawn through the resonator at a rate of 0.8 l min⁻¹, and the laser beam's power was square-wave modulated at the resonator's acoustic resonance frequency (1500 Hz). In this system, light is absorbed by particles in the sample air, inducing periodic heating of the gas, which generates an acoustic pressure wave. The acoustic signal detected by a microphone on one end of the resonator is thus proportional to the level of light absorption. The acoustic resonance frequency of the resonator and the resonator quality factor (gain) are determined by a piezo electrical disk on the other end of the resonator, which is used to calibrate the system. The laser's power is measured with an integrating sphere/photodetector. Strongly light-absorbing particles with low levels of scattering generated in a kerosene lamp operating in a fuel-rich mode were used to calibrate the instrument's absorption signal. In addition, in Paper I, the particles' light scattering coefficients were measured using a nephelometer incorporated into the PASS-3 instrument.

3.4.3 Size distribution measurement with a SMPS

In Paper I, a SMPS consisting of a DMA (model 3081 long, TSI Inc.) and a CPC (model 3010, TSI Inc.) was used to measure particle number size distributions. Before entering the DMA, the sample flow was diluted with nitrogen and the diluted aerosol sample was neutralized by a bipolar neutralizer (^{85}Kr).

In Papers II and III, the post-modification peak diameters of monodisperse soot samples were scanned using a DMA (DMA2, Vienna type, length 280 mm, inner/outer radius 25.0/33.3 mm, aerosol flow rate 2.25 l min^{-1} , and sheath flow rate 10.0 l min^{-1}) and a CPC (model 3775, TSI Inc., flow rate 0.3 l min^{-1}), which served as a scanning mobility particle sizer (SMPS) without a neutralizer.

3.4.4 Radiative intensity measurement with a narrow angle radiometer

A narrow angle radiometer was used to measure the radiative intensity of the flames in Paper I. This instrument measures the line-of-sight radiation in front of a probe⁷². The measurements were performed using a quartz window on the opposite side of the test rig as a cold background. The probe was traversed radially through the furnace in increments of 5 cm. The radiation was collimated in a long narrow tube (inner diameter: 10 mm) placed in a water-cooled titanium probe, and focused onto the detector (a thermopile), which was placed in the back-end of the probe. The detector housing was cooled with a separate cooling water circuit to maintain the detector at a constant temperature. The detector was calibrated with a high precision black body oven before each measurement campaign.

3.5 Data analysis

Details of the methods used for data analysis can be found in Papers I-V. The most important parameters considered in these studies are briefly discussed below.

3.5.1 Particle morphology

The mass equivalent diameter (D_{me}) of a particle is the diameter of a hypothetical spherical particle with the same mass as the actual particle, and can be computed as:

$$D_{me} = \sqrt[3]{\frac{6m_p}{\pi\rho_m}}, \quad (1)$$

where m_p is the particle's mass and ρ_m is its material density.

Changes in a particle's D_{me} upon coating were expressed in terms of the mass equivalent coating thickness (Δr_{me}):

$$\Delta r_{me} = \frac{D_{me} - D_{me,0}}{2}, \quad (2)$$

where $D_{me,0}$ and D_{me} are the mass equivalent diameters of the fresh and coated soot particles, respectively.

The mass-mobility exponent (Dfm) can be determined from:

$$m_p = K \cdot D_p^{Dfm}, \quad (3)$$

where D_p and K are the particle mobility diameter and an experimentally determined scaling prefactor, respectively. The value of K depends on the overlap between the primary spherules in the aggregate, and is related to the packing of the spherules in space.

The particle effective density (ρ_{eff}) can be computed as:

$$\rho_{eff} = \frac{6m_p}{\pi D_p^3}, \quad (4)$$

The dynamic shape factor (χ) can be calculated from the measured mobility diameter (D_p) and the volume equivalent diameter (D_{ve}):

$$\chi = \frac{D_p C_{ve}}{D_{ve} C_p}, \quad (5)$$

where C_{ve} and C_p are the Cunningham slip correction factors for particles with diameters D_{ve} and D_p , respectively. In-situ experimental determination of diameters D_{ve} is not currently possible, so soot aggregates are typically assumed to be free of internal voids such that $D_{ve} = D_{me}$.

The fraction of internal voids (F_i) and the fraction of open voids (F_o) in the soot aggregate are determined based on the following hypotheses: (i) in the case of soot coated with SOA, the open voids in the condensed material are preferentially filled prior to the onset of growth, and (ii) at the onset of growth, F_o is equal to the fraction of void space filled ($F_{vs,f}$), whereas $F_i = 1 - F_o$. The volume equivalent diameter including internal voids ($D_{ve,i}$) is then:

$$D_{ve,i} = \sqrt[3]{D_{me}^3 + D_p^3 F_{vs} F_i}, \quad (6)$$

With this value in hand, the *in-situ* dynamic shape factor can be derived using Eq. (5).

3.5.2 Optical properties

The complex refractive index (RI), $m = n - ik$, is the fundamental parameter determining the optical properties of particles; the real (n) and imaginary (k) parts represent scattering and absorption, respectively. According to Rayleigh theory, the absorption coefficient (b_{abs} , referred to as κ_λ in Paper I) is:

$$b_{abs} = \frac{36\pi nk}{(n^2 - k^2 + 2)^2 + 4n^2k^2} \frac{f_v}{\lambda}, \quad (7)$$

where f_v and λ are the volume concentration (volume fraction) of soot and the wavelength of incident light, respectively.

The single scattering albedo (SSA), which is scattering divided by extinction (i.e., the sum of absorption and scattering), can be calculated as:

$$SSA = \frac{b_{sca}}{b_{abs} + b_{sca}}, \quad (8)$$

where b_{sca} is the scattering coefficient (referred to as σ_λ in Paper I).

The mass absorption cross section (MAC) refers to the capacity to absorb light per unit mass. The MAC of BC particles is calculated from the absorption coefficient ($b_{abs,BC}$), number concentration (N_{BC}) and BC particle mass ($m_{p,BC}$) as follows:

$$MAC_{BC} = \frac{b_{abs,BC}}{m_{p,BC} N_{BC}}, \quad (9)$$

The MAC of light-absorbing organic particles co-emitted with BC (MAC_{Org}) can be calculated as:

$$MAC_T = f_{BC} MAC_{BC} + f_{Org} MAC_{Org} = \frac{b_{abs,T}}{m_{p,T} N_T}, \quad (10)$$

where MAC_T and MAC_{Org} are the MAC values of all light-absorbing particles and the organic mass fraction of particles, respectively. $b_{abs,T}$, N_T and $m_{p,T}$ are the absorption coefficient, number concentration, and particle mass associated with the total number of light-absorbing particles, respectively. f_{BC} and f_{Org} are the respective mass fractions of BC and organics.

The imaginary RI of POA (k_{POA}) can be calculated from the corresponding MAC of POA (MAC_{POA})⁸:

$$k_{POA} = \frac{\rho_{POA}\lambda}{4\pi\xi} MAC_{POA}, \quad (11)$$

where λ is the wavelength of light and ρ_{POA} is the material density of the POA (assumed to be 1.10 g cm⁻³). ξ is only weakly dependent on k_{POA} , representing the particulate effect compare to bulk solution. For organics where the real part of RI (n) is 1.5 and the particles are smaller than the wavelength of light, ξ ranges from 0.69 to 0.75⁹. In this study, the average value of ξ (i.e. 0.72) is used to determine k_{POA} .

The absorption cross sections (C_{abs}) of fresh soot or coated soot can be calculated as:

$$C_{abs} = \frac{b_{abs}}{N}, \quad (12)$$

where N is the particle number concentration.

The Ångström absorption exponent (AAE), which is generally used to characterize the spectral dependence of light absorption between two wavelengths (in this study, 405 and 781 nm), is calculated as:

$$AAE = -\frac{\ln(C_{abs,781}) - \ln(C_{abs,405})}{\ln(781) - \ln(405)}, \quad (13)$$

The absorption enhancement (E_{abs}) can be calculated based on the absorption cross sections of coated soot and fresh uncoated soot:

$$E_{abs} = \frac{C_{abs,coated}}{C_{abs,fresh}}, \quad (14)$$

Chapter IV

Results and discussion

The scientific content of this thesis includes characterizations of soot from industrial and laboratory scale flames, i.e. number size distributions, light absorption for two types of flames, and mass-mobility relationships for the evaporation of organics mixed with soot from lab-scale flames. It also includes (i) data on the morphological transformation and changes in optical properties of lab-scale flame soot induced by the condensation of sulfuric acid, SOA, and acidity-mediated SOA; and (ii) measurements of the effective density of ambient particles with other aerosol components such as SOA, sulfate and nitrate. The key findings are presented in five major sections: 4.1 Characteristics of industrial in-flame soot; 4.2 Characteristics of lab-scale flame soot; 4.3 Morphological transformation of soot; 4.4 Changes in optical properties of soot; 4.5 Effective densities of ambient particles during field measurements.

4.1 Characteristics of industrial in-flame soot

During the measurement campaign presented in Paper I, the particle size distribution of Flame A (an air-rich flame) and Flame B (a sooty flame, i.e. a fuel-rich flame) were measured using a SMPS. The soot particles in Flame A at Ports M2–M5 had diameters of 40–50 nm, suggesting that the soot existed as monomers or dimers at most^{8,73}. Conversely, the soot particles in Flame B had diameters of 100–150 nm, indicating the formation of aggregates. The soot volume fraction was three orders of magnitude higher in Flame B than in Flame A, which probably explains why primary soot spherules were more prone to coagulate into larger aggregates in the former case. While ports M3 and M2 were both positioned at heights corresponding to the fuel-rich region of Flame B, the soot particle size observed at port M3 (160 nm) was greater than at port M2 (140 nm), presumably because of coagulation, surface deposition and aggregation⁷³. Further downstream, where oxygen was entrained into the center of the flame, the soot particles started to be oxidized, causing the particle size to decrease between ports M3 (160 nm) and M5 (120 nm). No such variation in soot particle size was observed for Flame A.

Table 4.1 Measured absorption coefficients (κ), scattering coefficients (σ), and SSA values at the three wavelengths, and the corresponding AAE values for soot in Flame B (fuel-rich flame) at measurement ports M2 – M5.

Test case	κ_{405}	κ_{532}	κ_{781}	σ_{405}	σ_{532}	σ_{781}	SSA ₄₀₅	SSA ₅₃₂	SSA ₇₈₁	AAE
Flame B	(10 ⁻⁴)									
	[m ⁻¹]									
M2	57.3	34.2	19.7	8.6	3.3	0.7	0.13	0.09	0.03	1.61
M3	80.4	66.9	38.8	13.6	5.7	1.3	0.14	0.08	0.03	1.13
M4	40.8	33.0	21.1	6.4	2.6	0.6	0.14	0.07	0.03	1.01
M5	9.3	7.3	4.8	1.3	0.6	0.1	0.12	0.08	0.02	1.01

Table 4.1 presents the absorption coefficient, scattering coefficient, and SSA for Flame B at wavelengths of 405, 532, 781 nm, and the corresponding AAE values at each of the four measurement ports. At each port, the SSA decreased from ~0.13 to ~0.03 as the wavelength increased from 405 to 781 nm, i.e. on moving across the visible spectrum. According to Rayleigh theory⁷⁴, the absorption coefficient of soot should be significantly higher than its scattering coefficient in the infrared (IR) region, resulting in a near-zero SSA value. Interestingly, the AAE decreased from 1.61 to 1.01 between ports M2 and M5, indicating that soot formed at ports M2 and M3 in the fuel-rich zone of the flame was not mature yet and still had some organic nature (because the AAE was greater than 1), whereas the soot had become fully mature BC at port M5. The soot volume fraction was calculated from SMPS and PASS-3 data and four different complex refractive indices (RIs)⁷⁵⁻⁷⁸ from the literature that were used to fit the calculated absorption coefficients to the measured data (see detailed information in Paper I). The different RIs yielded slightly different soot volume fractions that were generally somewhat lower than those determined from the SMPS data. These differences can be attributed to limitations of the measurement systems and the chosen modeling strategy.

Figure 4.1 shows the measured absorption coefficients and the absorption coefficients calculated from the fitted soot volume fractions using the four different RIs as a function of wavenumber ($\eta = 1/\lambda$, where λ is the wavelength of the incident light). The agreement between the measured and calculated absorption coefficients was generally good, and both the measured and the modeled results showed higher absorption at shorter wavelengths.

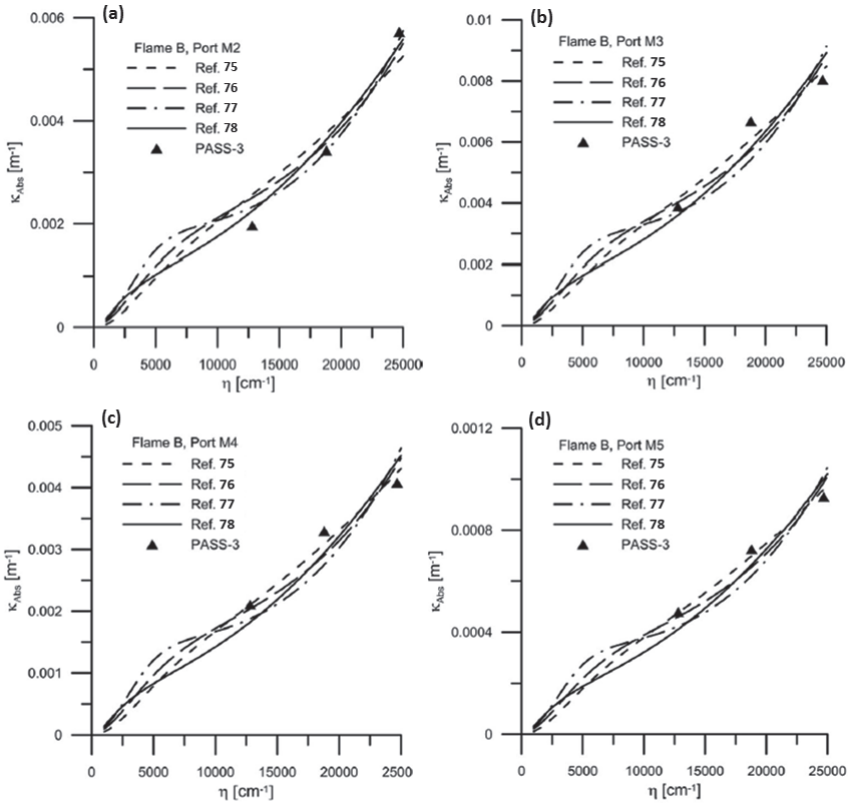


Figure 4.1 Measured and calculated absorption coefficients of soot in the fuel-rich Flame B at ports M2 (a), M3 (b), M4 (c), and M5 (d).

Figure 4.2 shows the measured and the modeled total radiative intensity at port M3 for Flame B using the four different complex RIs for soot. The position on the x -axis is the distance from the measurement port where the probe was inserted. The inputs to the radiation model⁷⁹ are the measured temperature and gas and particle concentrations. The Malkmus statistical narrow band model⁸⁰ was used to estimate the gas properties, and Rayleigh theory was used to calculate the soot's optical properties. When the quartz window was placed 800 mm from the port, the detected radiative intensity was low. As the window was moved towards the port, the amount of hot gas and particles in the probe's line of sight increased, and therefore so did the detected radiative intensity of the flame. When the probe was around 300 mm from the pot, the absorption of radiation by the cold gas outside the flame reduced the observed radiative intensity. Overall, the measured and modelled values agreed well and the differences between them can be attributed to the limitations of the experimental system and the chosen modeling strategy.

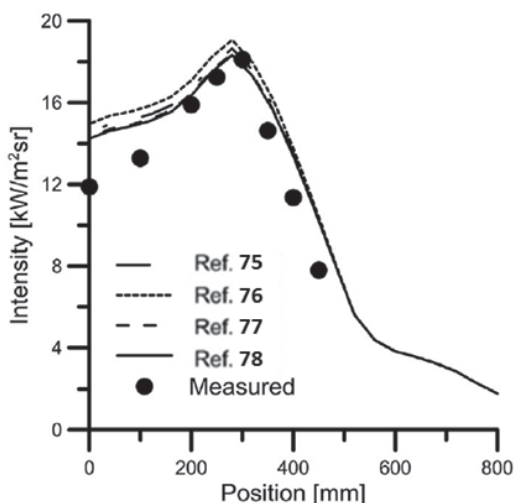


Figure 4.2 Measured and modeled total radiative intensity profiles for Flame B at port M3 with different complex RIs.

4.2 Characteristics of lab-scale flame soot

4.2.1 Composition and mixing state of soot

Section 4.1 shows the properties of fresh soot from industrial flames. However, to study the transformation of soot under controlled conditions, laboratory experiments are needed. Paper II examined the characteristics of soot particles of five different sizes (75, 100, 150, 200 and 250 nm) from three lab-scale propane flames (Exp. F1, Exp. F2 and Exp. F3). Two main components were found in particles of all five sizes: BC and POA. The POA mass fraction contributed 20–40% of the total particle mass (BC+POA) in soot from all three flames. The diffusion-to-premixing air ratio (d/p ratio) may have affected the mechanism of POA formation and the size dependence of the POA mass fraction because the POA mass fraction was strongly size-dependent when the d/p ratio was small (13.8) but negligibly size-dependent when the d/p ratio increased to 19.9. This suggests that the formation of smaller POA particles may have been favored by reductions in the d/p ratio. The POA mass fractions in the largest (250 nm) soot particles were very similar for all three flames, indicating that POA of this size was not significantly influenced by changes in the proportions of premixing air and diffusion air.

The scaling prefactor (K) and the mass mobility exponent (D_{fm}) were determined for the five soot particle sizes in each flame at 25 °C and 400 °C. The D_{fm} values ranged between 2.13 and 2.34, in keeping with earlier reports^{17,26}, indicating that the soot had

a non-spherical aggregate structure. The Sorensen model¹⁶ (see Paper II for details) was used to determine the diameter of a primary spherule (d_{pp}) and the number of primary spherules in a soot aggregate (N_{pp}). The results obtained were again consistent with previous findings⁶⁷: the d_{pp} of particles in all three flames was essentially constant over the entire D_p range. Reducing the proportion of premixing air had no effect on the d_{pp} , but reducing that of diffusion air led to the formation of larger primary spherules (~ 26 – 29 nm) in BC aggregates of 100 nm or above. The d_{pp} obtained in this study (~ 20 – 29 nm) was comparable to those for diesel soot⁶⁷ and Mini-CAST soot formed under fuel-lean conditions⁸¹, but smaller than that for soot from the oxy-fuel test rig discussed in Paper I (40–50 nm, see section 4.1). This may be due to the use of different burning conditions and measurement techniques.

The size-resolved mixing state of BC and POA was determined by measuring the number concentration and mass of particles from the flame exhaust using the NTD (25 °C) and TD (400 °C) setups with VTDMA⁸². Figure 4.3 shows the number size distributions of particles in the three flames at 25 °C and 400 °C, and the mass concentration and mixing states of the size-resolved soot in all three flames at 25 °C.

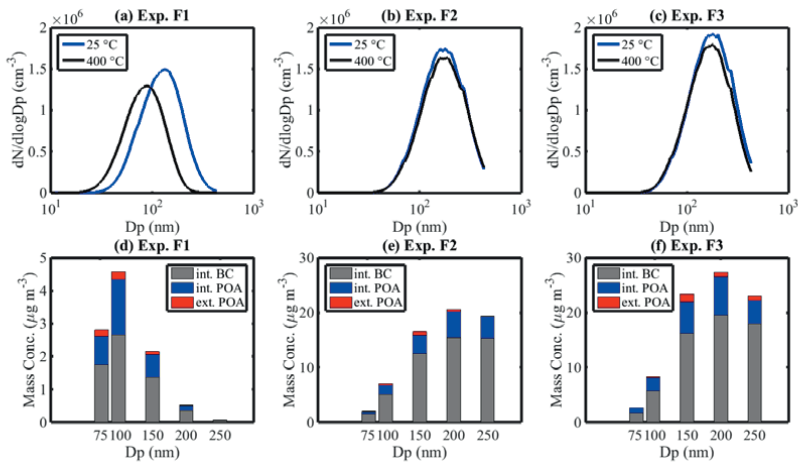


Figure 4.3 Top: Number size distributions of particles in (a) Exp. F1, (b) Exp. F2 and (c) Exp. F3 flames at 25 °C and 400 °C. Bottom: Mass concentrations and mixing states of size-resolved soot particles in (d) Exp. F1, (e) Exp. F2 and (f) Exp. F3 flames at 25 °C.

As shown in Figure 4.3 (a), the polydisperse soot in the Exp. F1 flame had a log-normal size distribution with a mode peak at 130 nm and a total number concentration of $7.8 \times 10^5 \text{ cm}^{-3}$ at 25 °C. When this soot population was heated to 400 °C, its mode peak size and total number concentration fell significantly to 90 nm and $6.4 \times 10^5 \text{ cm}^{-3}$, respectively, suggesting that the soot consisted of both externally mixed POA ($\sim 18\%$ by number, which was evaporated completely) and internally mixed BC and POA ($\sim 82\%$ by number, which shrank from 130 nm to 90 nm). In

keeping with the number fraction data, the mass fraction measurements in Figure 4.3 (d) show that POA was mainly internally mixed with BC at 25 °C. The mass fraction of externally mixed POA decreased from 7% for 75 nm particles to 2% for 250 nm particles, indicating that externally mixed POA was mainly formed in particles smaller than 75 nm. Previous studies showed that primary organic carbon was only formed in small particles of 1–10 nm by homogeneous nucleation of organic vapors or hydrocarbon combustion reactions^{83,84}, and grew by condensation of PAH vapors, making it difficult for these externally mixed POA particles to grow appreciably.

The soot in Exp. F2 and Exp. F3 flames exhibited similar number size distributions with a larger peak mode (~175 nm). The peak mode of the soot population in these flames was unaffected by heating, indicating that no significant restructuring (collapse) of the soot cores occurred, presumably because of the smaller mass fraction of internally mixed POA compared to that in Exp. F1 soot. Because the mass fraction of POA was small, the surface tension force exerted by the POA was lower than that required for restructuring of the soot aggregate. As in Exp. F1 flame, the POA in Exp. F2 and Exp. F3 flames was mainly internally mixed with BC; the mass fraction of externally mixed POA was very small (0–6%).

4.2.2 Morphology of soot

When soot particles containing BC and POA were heated to 400 °C, changes in the morphological structure of the soot were probably mainly influenced by the evaporation of POA. A framework was developed to quantify the state of the morphological transformation of soot exposed to heating. This transformation involves the shrinkage of the soot particles resulting from the removal of condensed material from the surface and voids, as shown in Figure 4.4. In this figure, the particle mobility diameter shrink factor (Sfd , i.e. the ratio of the current mobility diameter to the initial mobility diameter) is plotted as a function of the reduction in the coating thickness (Δr_{me}). The ideal shrink line (shown as a solid black line) represents the trend expected for the removal of condensed material from a perfect incompressible solid sphere surface with the same mass equivalent diameter as the BC core.

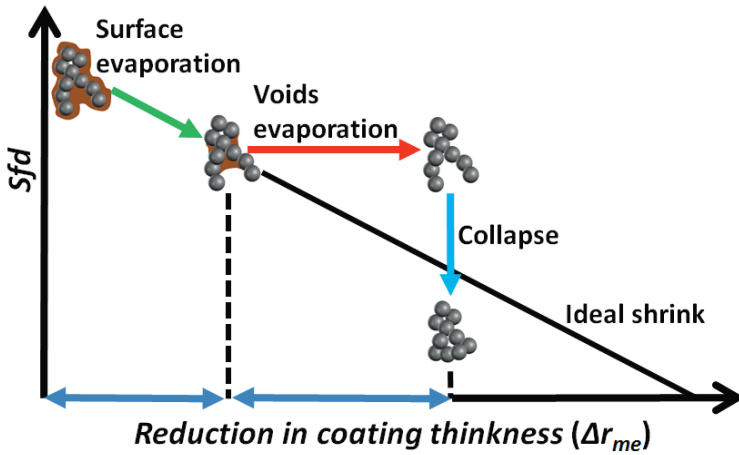


Figure 4.4 Framework for quantifying the state of the morphological transformation of soot upon heating.

The framework is based on three processes: (i) removal of the POA layer coating the BC surface (Surface evaporation), which is characterized by a decrease in Sfd as Δr_{me} increases, along or parallel to the ideal shrink line; (ii) removal of POA from voids in the BC aggregate (Voids evaporation), which is characterized by an unchanging Sfd as Δr_{me} increases; and (iii) shrinkage (or reduction in the mobility diameter) due to collapse of the BC core. BC core collapse is defined as a reduction in the mobility diameter by rearrangement of primary spherules induced by surface tension force exerted by evaporating POA, but not due to evaporation of material mass. This collapse is characterized by a sudden sharp decrease in Sfd parallel to the y-axis. Processes (i), (ii) and (iii) are represented by solid green, red and blue lines, respectively, in Figure 4.4.

By plotting the Sfd and Δr_{me} values (collectively referred to as a “measurement point”) of a real soot particle on a graph such as that shown in Figure 4.4, one can predict its shrinkage behavior. The pathway to a given measurement point will involve some combination of these three processes. If the measurement point is above the ideal shrink line, some material must have condensed in the particle’s voids, and preferentially in the open voids; it is not possible for any coating to condense on the surface without filling at least some voids. In fact, open voids in a soot particle are likely to be filled before surface growth occurs, providing a base for material deposition on the surface. Therefore, a point above the ideal line suggests that the BC may collapse but will not necessarily do so. If the measurement point is on the ideal shrink line, then all three pathways (i.e. surface evaporation, voids evaporation, collapse, or some combination thereof) are possible. The evaporated material may be partially on the surface, or partially/entirely in the voids. If the evaporated material is all in the voids and none is on the surface, the reduction in the BC core’s volume

must equal to the volume of material lost from voids. If the measurement point is below the ideal shrink line, the BC core must have partially collapsed, and the minimum collapse which equivalents to the corresponding ΔSfd below the ideal line will be inevitable. The evaporated material may have been lost entirely from voids or partially from both, but it can never be accommodated entirely for the surface growth because the total void volume contains the surface of the voids. In this study, collapse of the BC core reduced the mobility diameter of soot from Exp. F1 flame by 10–16%, but decreases of only 7% were observed for Exp. F2 and Exp. F3 flames. Therefore, given the measurement error of DMA (~5%), particles in Exp. F2 and Exp. F3 exhibited very low levels of collapse – much lower than those of Exp. F1 particles.

The *in-situ* dynamic shape factor (χ) can be derived in a way that accounts for internal voids using Eq. (5). Figure 4.5 shows the χ values of particles from Exp. F1 at 25 °C and 400 °C without accounting for internal voids, and at 400 °C with internal voids accounted for, as functions of D_p . When accounting for internal voids, D_{ve} was larger than D_{me} and the resulting χ was smaller than that obtained when internal voids were neglected. Generally, χ increased with the D_p of particles without internal voids at both 25 °C and 400 °C. The χ of BC at 400 °C with internal voids was significantly smaller (1.04–1.08) than that without internal voids. This indicates that accounting for internal voids yields near-spherical BC particles. The χ values of pure BC decreased significantly when internal voids were included in the calculation, indicating that internal voids occupied significant space and the traditional method is inadequate for predicting *in-situ* χ values.

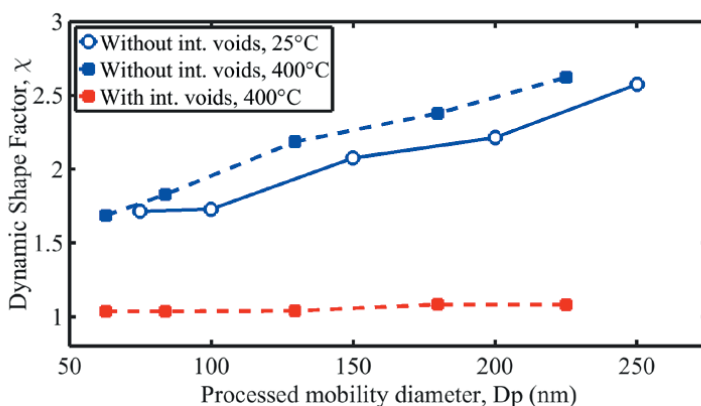


Figure 4.5 Dynamic shape factors (χ) of particles from Exp. F1 without accounting for internal voids at 25 °C, and with and without accounting for internal voids at 400 °C.

4.2.3 Absorption properties of BC and POA

The AAE is a parameter that describes the wavelength-dependence of light absorption for particles of various sizes. The average $AAE_{405/781}$ values (calculated from absorption measurements at 405 and 781 nm) for BC+POA from the Exp. F1, Exp. F2 and Exp. F3 flames were 2.06 ± 0.11 , 1.65 ± 0.08 and 1.84 ± 0.06 , respectively; the corresponding values for BC alone were 1.01 ± 0.12 , 1.08 ± 0.11 , and 1.28 ± 0.07 . These results indicate that all sizes of soot particles in all three flames had significant contents of light-absorbing POA (i.e. BrC). However, the AAE value of mature soot from the oxy-fuel test rig used in Paper I was only 1.01 (see section 4.1), indicating that POA was not present in the soot from the test rig due to its high operating temperature.

The MAC values for BC from all three flames were similar at each of the three considered wavelengths (405, 532 and 781 nm). The recommended reference MAC value of BC ($7.5 \text{ m}^2 \text{ g}^{-1}$) was used to calculate theoretical MAC values at each wavelength assuming a theoretical AAE value of 1.0. The measured MAC values at each wavelength were all smaller than these theoretical values. These results indicate that the specific combustion settings of the studied flames did not affect the absorptive nature of pure BC, but the BC particles were richer in sp^3 -hybridized carbons (which do not absorb visible light) than predicted based on the reference values, and had fewer sp^2 -hybridized carbons (which absorb visible light strongly).

The MAC values of POA in all three flames were also estimated, revealing that the MACs for BC were higher than those for POA at all three wavelengths. However, at the wavelength of 405 nm, the MAC value of BrC ($5 \text{ m}^2 \text{ g}^{-1}$) under a certain flame setting (Exp. F2) was comparable to that of BC ($8\text{--}9 \text{ m}^2 \text{ g}^{-1}$). The MAC values and the corresponding imaginary part of the RI for POA (k_{POA} , derived from Eq. (11)) for all three flames are shown as functions of the wavelength in Figure 4.6, together with literature data for POA formed during propane combustion (Kim et al.²⁰ and Lu et al.²²) and extracted from biomass samples (Kirchstetter et al.⁹). At the short wavelength of 405 nm, the POA from all three flames examined in this study exhibited strong absorption, which decreased significantly at longer wavelengths. The particles in the Exp. F1 and Exp. F3 flames had the same MAC at 405 nm, which was lower than that for Exp. F2 flame particles. This indicates that the flame conditions had a significant influence on the MAC of POA. Differences in the molecular composition of POA originating from different emission sources could cause differences in MAC and k_{POA} values at wavelengths below 530 nm^{22,81}. The absorption of POA increases almost continuously with the extent of π -system conjugation⁸⁵, indicating that the particles from the Exp. F2 flame may have had higher contents of polycyclic aromatic hydrocarbons (PAH) or PAH-like materials than those from the Exp. F1 and Exp. F3 flames.

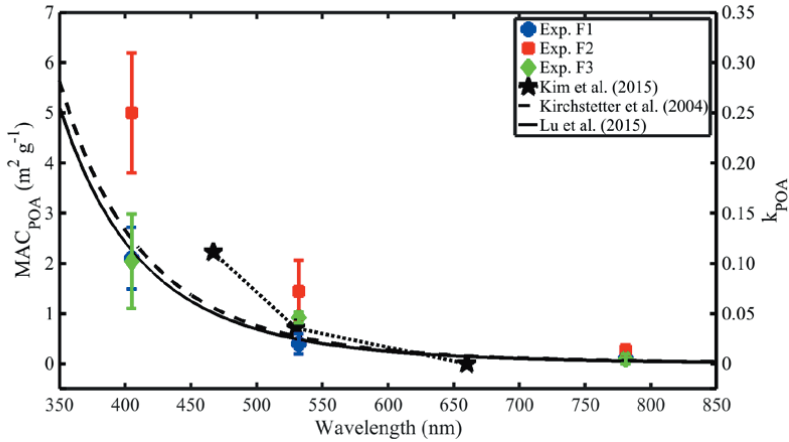


Figure 4.6 MAC values and estimated imaginary refractive indices of POA (k_{POA}) as functions of the wavelength.

4.3 Morphological transformation of soot

4.3.1 Framework to quantify the morphology

Paper III examined the morphological transformation of soot from the Exp. F1 flame described in Paper II. A framework was developed to quantify the state of the morphological transformation of soot during condensation process, i.e., the utilization of material for filling voids and surface growth, as shown in Figure 4.7. Figure 4.7 (a) shows the particle diameter growth factor (Gfd , the ratio of the current and initial mobility diameters) as a function of the mass equivalent coating thickness (Δr_{me}) at specific measurement points. The concept of ideal growth, which is represented by a black solid line, describes the mobility diameter growth of a perfect incompressible solid sphere with the same initial mobility diameter and mass as the fresh soot particle when material condenses on it. Real soot particles are neither spherical nor incompressible because they are aggregates of primary spherules and thus contain voids, so the deviations between the experimental measurements and the ideal growth line can be interpreted to quantify the filling of voids and growth on the particle surface. The framework was developed based on the hypothesis that when material condenses on soot, the void filling can be described by a line parallel to the x-axis, while the growth can be described by changes in Gfd parallel to the ideal growth line. The coating thicknesses for void filling ($\Delta r_{me,f}$) and particle growth ($\Delta r_{me,g}$) are indicated by the red arrow (parallel to the x-axis) and the green arrow (parallel to the ideal growth line), respectively. From this framework, the fraction of void space filled ($F_{vs,f}$), volumes of material utilized for void filling (V_f) and diameter growth (V_g), and the percentages of material utilized for filling (P_f) and growth (P_g)

can be derived based on the assumption of a concentric core-shell structure evolving during the process of condensation (see Figure 4.7 (b) for an illustration and Paper III for details).

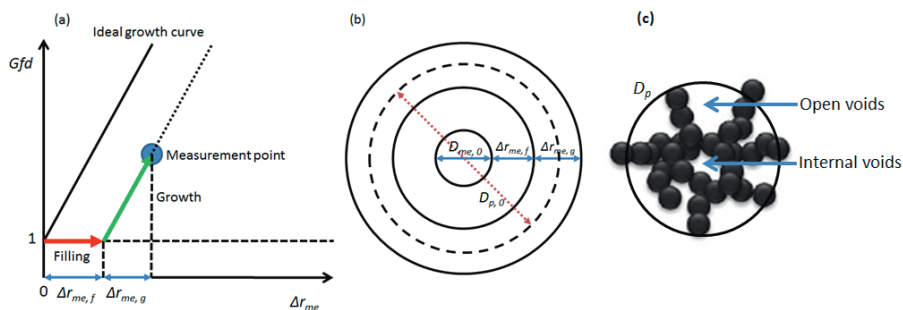


Figure 4.7 Illustration of the framework for quantifying the morphological transformation and structure of a soot aggregate with open voids and internal voids.

4.3.2 Particle void-filling and diameter growth

The morphological transformation of a soot aggregate upon condensation of materials can be described in terms of the mobility diameter growth factor (Gfd). To give an example, Figure 4.8 shows the changes in Gfd of soot particles with an initial mobility diameter of 200 nm as a function of the mass equivalent coating thickness (Δr_{me}). In Figure 4.8, the black dashed line represents the ideal growth line, and the pie charts denoting each data point show the chemical composition of fresh and processed soot particles. The black, red, and green colors in each pie chart represent the mass fraction of BC, sulfuric acid, and organics, respectively. The morphological transformation of soot particles is hypothesized to result from the: (i) filling of voids in the soot aggregates; (ii) increases in mobility diameter; and (iii) rearrangement of primary spherules within the soot aggregate (i.e., collapse) due to surface tension force exerted by the condensed materials. Both the mass and the mobility diameter of the particle will be increased by condensation of materials. However, adding material to the void space of soot particles will increase their mass but leave their mobility diameter unchanged (or possible cause it to fall via collapse). The real morphological transformation of the soot particles will result from a combination of two or more of these processes. The purple lines in Figure 4.8 show changes in Gfd associated with different condensed materials, which can be summarized as follows: (i) lines parallel to the x-axis indicate that all condensed materials were utilized for filling voids; (ii) lines parallel to the ideal growth line indicate that all condensed materials were utilized for mobility diameter growth; (iii) negative slopes indicate a combination of void space filling and soot particle collapse. The description of the morphological transformation in terms of Gfd reveals a clear dependence of

morphological change on particle size. A detailed discussion of this behavior for each particle size class can be found in Paper III.

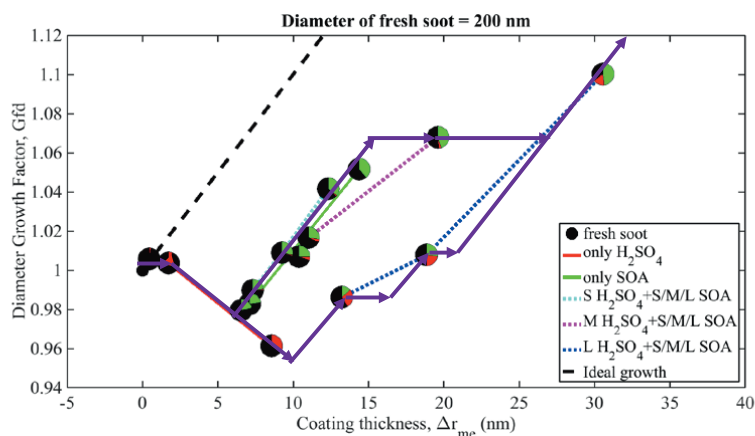


Figure 4.8 Changes in the mobility diameter growth factor (G_{fd}) of soot particles with an initial mobility diameter of 200 nm as a function of the mass equivalent coating thickness (Δr_{me}).

With regard to their microphysical structure, the soot aggregates considered here were assumed to primarily contain two types of voids: (i) internal voids, i.e., space shielded by soot primary spherules; and (ii) open voids, i.e., space open to the atmosphere (see Figure 4.7 (c)). Both types of voids were assumed to lie within a hypothetical sphere with same mobility diameter as the fresh soot particle. The open voids were assumed to be filled in preference to internal voids during vapor condensation due to the shielding effect of the primary spherules. The narrow openings between primary spherules probably bottlenecked access to the internal voids, preventing the entry of material into the internal voids except for high masses. The step-wise filling and subsequent growth processes were thus controlled by these occurrences and proceeded until all the voids were filled.

Previous studies on the morphological transformation of soot using similar techniques^{31,41} were also evaluated using the framework described above and compared to this study. Figure 4.9 shows the G_{fd} as a function of Δr_{me} for the 100 nm soot transformations observed in this study and in the smog chamber experiments of Guo et al.⁴¹ and Qiu et al.³¹. The major difference between this study and those cited is that in the present work a flow tube was used rather than a smog chamber. Particle growth in smog chambers is dynamic, so the particles' properties (including their mobility diameters and masses) were measured at 40 minute intervals while the particles were growing continuously. This growth could affect the reliability of the mapping of the particle mass and the mobility diameter, leading to overestimation of Δr_{me} . Nevertheless, the features associated with the morphological transformation (i.e., void filling and diameter growth) of the soot particles in the smog chambers was

described fairly well by the new framework. The framework indicated that the soot in the earlier studies primarily contained open voids (84–95%), as indicated by the curves shown in Figure 4.9. In the smog chamber studies, void filling and diameter growth occurred sequentially but over very short time periods, indicating that internal voids were relatively easy to fill. These results show that the framework developed in this study is quite robust and can be used to evaluate measured masses and mobility diameters to interpret the morphological transformations of soot induced by various types of condensed materials.

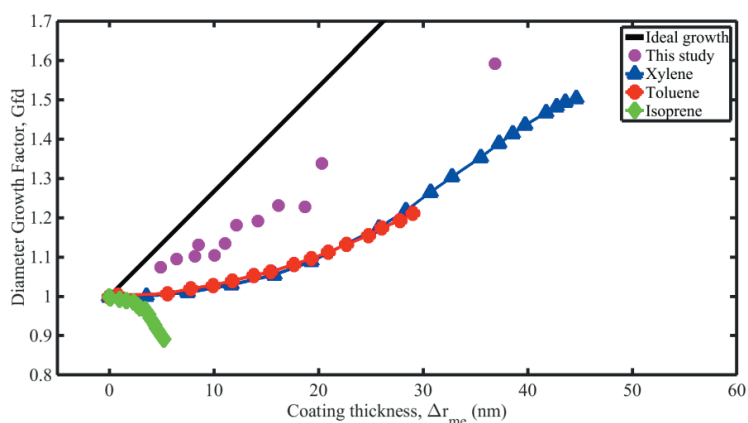


Figure 4.9 Changes in the mobility diameter growth factor (Gfd) of soot particles with an initial mobility diameter of 100 nm as a function of the mass equivalent coating thickness (Δr_{me}), as obtained in this study and reported in the literature.

4.3.3 Dynamic shape factor

The shapes of both fresh and coated soot particles can be represented by the dynamic shape factor χ . Figure 4.10 shows χ as a function of Δr_{me} for 200 nm soot and the same soot cores coated with pure sulfuric acid, pure SOA, or acidity-mediated SOA. The blue points represent the results of calculations using Eq. (5) under the assumption of no internal voids, while red points and lines represent the results of calculations assuming the presence of internal voids. The total void space of the soot particles examined in this study was dominated by internal voids (~90%). Therefore, the χ values obtained by assuming the presence of internal voids were significantly lower than those obtained by assuming no internal voids. Under the latter assumption, the equivalent volume is taken to equal to the sum of the primary spherules' volumes, with no consideration of voids, so the *in-situ* morphology of the soot aggregate is neglected. The findings presented here highlight the serious shortcomings of the assumption that $D_{ve} = D_{me}$. The χ values reported in previous studies based on the assumption of no internal voids thus appear to be consistent with each other for the wrong reason. In reality, and as confirmed in this study, soot

aggregates will inevitably contain internal voids. The experimental setup used to develop the framework presented herein, i.e., a flow tube integrated with a DMA-APM, can be used to determine the precise *in-situ* morphological characteristics of soot particles and describe their transformation following the condensation of (in)organic materials.

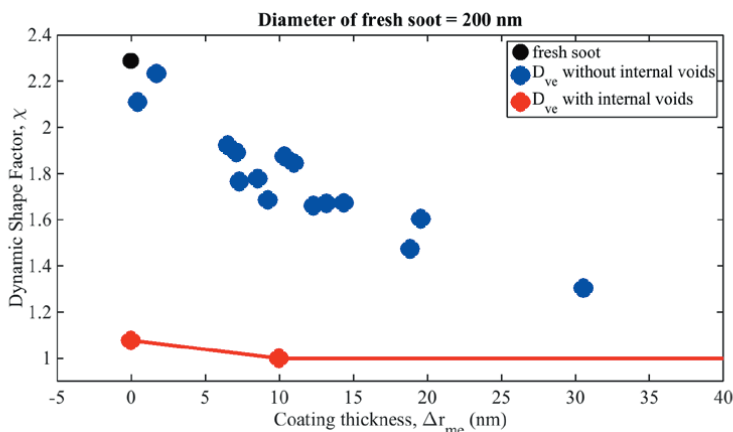


Figure 4.10 Changes in the dynamic shape factor (χ) of fresh and processed 200 nm soot particles as a function of the mass equivalent coating thickness (Δr_{me}).

4.4 Changes in optical properties of soot

The current understanding of the changes in optical properties of soot due to condensation of materials is largely based on the core-shell Mie theory of light absorption enhancement. In the Mie theory, the enhancement of light absorption is modeled as function of soot particle size, the refractive indices of the soot and condensed materials, and the coating thickness or the amount of the condensed material. In this study, I explored and evaluated factors not considered in the Mie theory that may influence the light absorption of coated soot particles. This led to new observations and theoretical insights showing that reactions between the soot and condensed material have important effects. In other words, the chemical nature of the condensing material can significantly influence the soot particles' optical properties. Also, I have discovered that oxidants such as ozone, can play important roles in the changes in optical properties of soot as it ages in the atmosphere.

4.4.1 Effects of sulfuric acid condensation on BC

When soot particles passed through the mixing chamber, sulfuric acid vapor preferentially condensed in the open voids first, and then sequentially condensed in the internal voids as described in section 4.3. The resulting changes in the particles'

morphological properties resulting from void filling and growth in particle mobility diameter, and the changes in their optical properties – especially absorption coefficient (b_{abs}) – were investigated simultaneously to clarify how condensation of materials on BC enhances its absorption. The absorption cross section (C_{abs}) of four sizes of BC particles (75, 100, 150, 200 nm) at 781 nm after the condensation of sulfuric acid is plotted as a function of the mass equivalent coating thickness (Δr_{me}) in Figure 4.11. The results were not consistent with the prediction of Mie theory (as shown by Mie model lines in Figure 4.11). After coating with a small amount of sulfuric acid, the C_{abs} of BC fell sharply – by 25%, 22%, 26%, and 8%, respectively, for 75, 100, 150, and 200 nm BC particles. As more sulfuric acid condensed on the BC, its C_{abs} began to increase, but still generally remained below the Mie model line. These observations were attributed to the combined effects of two competing processes: (i) the reduction of C_{abs} by the chemical reaction of sulfuric acid with carbon atoms, and (ii) the lensing effect, i.e. the enhancement of C_{abs} due to interactions between electromagnetic wave and the condensed material, which acted as an equivalent lens for the D_{me} of the BC core, focusing light onto the core. The latter effect is well described by the core-shell Mie model, but the former is not. By considering both of these processes, I developed a framework for quantifying their individual effects with the following theoretical basis.

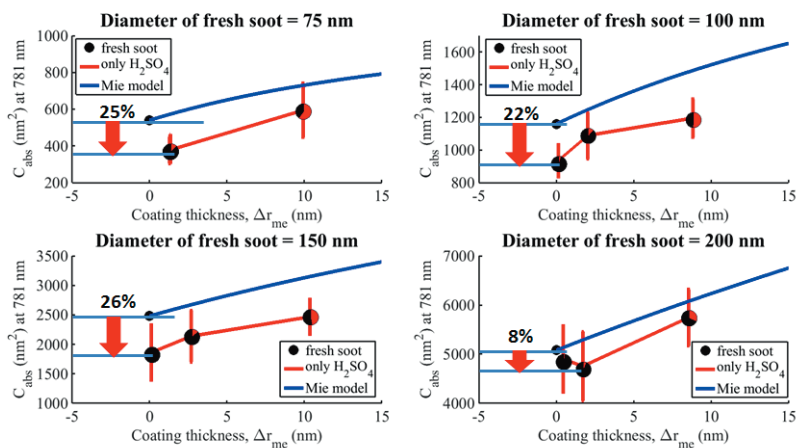


Figure 4.11 Absorption cross sections (C_{abs}) of four BC particle sizes (75, 100, 150, 200 nm) at 781 nm upon the condensation of sulfuric acid as a function of the mass equivalent coating thickness (Δr_{me}).

The electronic properties of carbon atoms on the surface of soot particles are hypothesized to be changed by reaction with sulfuric acid. Some previous studies^{86,87} have suggested that (i) the loss of sulfuric acid to soot particles is irreversible and the uptake of sulfuric acid on soot particles proceeds efficiently under atmospheric conditions⁸⁸; and (ii) the carbon atoms in graphite-like sheets in soot become ionic and bind bisulfate ions at high concentrations of sulfuric acid (>85%)⁸⁹. This reaction

is proposed to involve the auto-ionization of free H_2SO_4 molecules, i.e., $2\text{H}_2\text{SO}_4 \rightarrow \text{H}_3\text{SO}_4^+ + \text{HSO}_4^-$. The resulting free H_3SO_4^+ molecules can then protonate carbon atoms. The overall reaction of sp^2 hybridized carbon atoms with H_2SO_4 can be expressed as: $\text{C}_n + \text{H}_2\text{SO}_4 \rightarrow \text{C}_n^+ + \text{HSO}_4^-$. In addition, graphite has been observed to permit non-oxidative intercalation of Brønsted acids such as sulfuric acid, forming a first-stage structure of intercalated molecules between adjacent graphene layers⁹⁰. These graphite intercalation compounds form via the insertion of guest molecules or ions between sp^2 -bonded carbon layers, allowing the inserted compounds to interact directly with the π electrons of the graphene sheet. A key mechanistic point is that the delocalized π electrons on the BC surface, which are largely responsible for visible light absorption, are removed from the π system by reaction with protons, leading to a reduction in C_{abs} when small amounts of sulfuric acid condense on the BC surface. As more sulfuric acid condenses on the BC particle, its C_{abs} increases, indicating that the lensing effect begins to compensate for the reduction in C_{abs} due to π electron removal. In conclusion, the measured C_{abs} is governed by two opposing processes: π electron removal reduces C_{abs} but the lensing effect increases it.

4.4.2 Lensing effect and the role of condensed material

Interestingly, the absorption enhancement (E_{abs}) of BC coated with pure SOA at 405 nm was somewhat higher (~15–20%) than predicted by the Mie theory. However, the C_{abs} of all sizes of BC particles at 532 nm and 781 nm was well predicted by Mie theory. This suggests that Mie theory can explain the enhancement due to lensing at 532 nm and 781 nm. Two hypotheses were proposed to explain the greater absorption enhancement at 405 nm: (i) formation of optically active functional groups in the SOA (BrC) that absorbed light at short wavelengths, and (ii) reactions of ozone with the soot surface that added light-absorbing functional groups to the soot, and occurred simultaneously during the formation and condensation of SOA in the flow tube experiments. However, many studies^{21,91,92} on SOA derived from limonene ozonolysis have shown that such aerosols are mainly non-absorbing or absorb very weakly at 405 nm. On the other hand, some studies^{93,94} have shown that rapid reactions of ozone with soot surface sites can produce CO_2 and form carboxylic acids or similar oxygenated functional groups on the soot surface. This occurs when ozone attacks the carbon atoms on the outer edges of the sp^2 hybridized graphene sheet and oxygen atoms are added, leading to the removal of one sp^3 hybridized carbon center and its replacement by a sp^2 hybridized carbon-oxygen bond. Thus, overall, the number of π electrons is increased by such additions of oxygen. These new π electrons can absorb additional light, thereby enhancing the light absorption of BC particles. It should be noted that these added π electrons have a higher binding energy to the graphene sheet because the C–O π bond is stronger than the highest energy carbon-carbon π bonds of the soot particles⁹⁵. Therefore, the enhancement is only observed at 405 nm.

Figure 4.12 shows the absorption cross section (C_{abs}) of 100 nm BC particles as a function of the coating thickness (Δr_{me}) under the experimental conditions described in section 3.3.2. The lensing effect is revealed by the red dotted line (showing the results for coating with pure sulfuric acid), the green dotted line (pure SOA) and the black dotted line (acidity-mediated SOA). It is obvious that most of the experimental data points are below the corresponding lines predicted by the Mie theory. The divergence of the observations from the model lines occurs because of (i) the enhancement due to the condensed material's lensing effect; (ii) the reduction in absorption due to the reaction of sulfuric acid with carbon atoms on the graphene sheets of soot; (iii) the enhancement due to formation of BrC in the acidity-mediated SOA; (iv) the enhancement due to the heterogeneous reaction of ozone with carbon atoms on the graphene sheets of soot. Depending on the order and/or amount of the condensed materials, these processes may compete with or complement each other. The observed enhancement in any given case will thus result from a combination/permutation of one or more processes. The contributions of the four processes mentioned above can be quantified using the framework described in the following section.

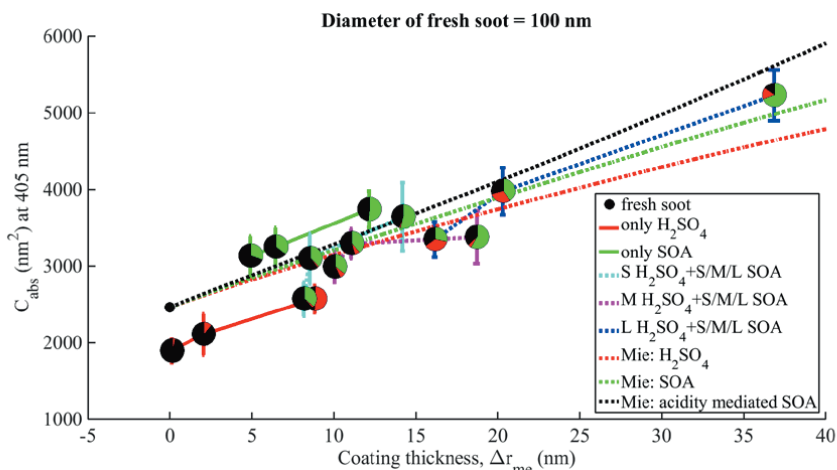


Figure 4.12 Absorption cross section (C_{abs}) of fresh and processed 100-nm BC particles at 405 nm as a function of the mass equivalent coating thickness (Δr_{me}). The RI values for BC, sulfuric acid, SOA, and acidity-mediated SOA at 405 nm are 2.1 – 0.5i, 1.42 – 0i, 1.5 – 0i, 1.5 – 0.01i, respectively.

4.4.3 Framework to quantify the changes in optical properties

A framework was developed for quantifying the changes in optical properties of soot during condensation process. By using an ideal sphere as a model, i.e., a sphere with the same mass equivalent diameter as the BC particles of interest, the core-shell Mie theory can accurately predict the absorption enhancement due to the lensing effect

that results from the condensation of a material with a known RI. In addition, it is hypothesized that all condensed materials form identical lenses, so the only differences in their lensing effects are those resulting from differences in their RI values. In this work, the RI value of pure BC was optimized using Mie theory subject to the constraints of the experimental measurements, while RI values of pure substances such as sulfuric acid and pure SOA were obtained from the literature⁹¹. Because the observed C_{abs} value is taken to reflect one or more of the processes listed in section 4.4.2, it is assumed to be the sum of the contribution of each process and can be quantified as:

$$\begin{cases} C_{abs,obs} = C_{abs,BC} + \sum \Delta C_{abs,process} \\ \sum \Delta C_{abs,process} = \Delta C_{abs,lens} + \Delta C_{abs,H_2SO_4\ reaction} + \Delta C_{abs,O_3\ reaction} + \Delta C_{abs,BrC} \end{cases}, \quad (15)$$

where $\Delta C_{abs,process}$ is the contribution to the absorption cross section (C_{abs}) of BC of an individual process such as lensing effect ($\Delta C_{abs,lens}$), reaction of sulfuric acid with BC surface ($\Delta C_{abs,H_2SO_4\ reaction}$), heterogeneous chemistry of oxidant (ozone) on the BC surface ($\Delta C_{abs,O_3\ reaction}$), and the formation of BrC in acidity-mediated SOA ($\Delta C_{abs,BrC}$). This framework can be used to evaluate the contribution of various processes to light absorption (both positive and negative), and possibly to reconcile the conflicting results of field observations, laboratory measurements, and model predictions^{44,46}.

Mie theory with optimized RI values can be used to calculate the ideal absorption for BC cores and different types of condensed materials, i.e., sulfuric acid, pure SOA, and acidity-mediated SOA. The lensing effects ($C_{abs,lens}$) of condensed materials are assumed to follow the lines of the Mie model. Any reduction of C_{abs} relative to the C_{abs} of fresh BC is attributed to the chemical reaction of sulfuric acid with carbon atoms, and any increase of C_{abs} of SOA relative to the line of the Mie model of pure SOA is caused by the chemical reaction of ozone with BC. The increase of C_{abs} predicted by Mie model of acidity-mediated SOA relative to that of pure SOA results from the formation of BrC. For instance, Table 4.2 shows the effect of different processes on the absorption cross section (C_{abs}) at 405 nm for soot particles of 75, 100, 150, and 200 nm coated with large levels of sulfuric acid and SOA. The percentages in the table represent the contribution of each process relative to the C_{abs} of pure BC ($\Delta C_{abs,process}/C_{abs,BC}$). The table shows that for all soot particle sizes, sulfuric acid lensing, SOA lensing, the effect of ozone, and the effect of BrC formation in acidity-mediated SOA all enhance the light absorption of BC, but the sulfuric acid reaction reduces light absorption.

Table 4.2 Effects of different processes on the absorption cross section (C_{abs}) at 405 nm of 75, 100, 150 and 200 nm soot particles coated with large levels of sulfuric acid and SOA.

Soot size (nm)	Effect of sulfuric acid lensing (%)	Effect of SOA lensing (%)	Effect of sulfuric acid reaction (%)	Effect of ozone reaction (%)	Effect of BrC formation (%)
75	29	139	-26	18	25
100	25	97	-44	16	23
150	25	76	-21	15	10
200	16	53	-9	20	8

4.5 Effective densities of ambient particles during field measurements

Sections 4.2–4.4 (Paper II-IV) describes findings from laboratory work on the characterization and transformation of fresh soot. This section describes the properties of soot coated with other aerosol components measured under ambient conditions in Beijing during summertime in 2016. As part of an intensive field measurement campaign for the Photochemical Smog in China project, a field experiment investigating soot morphology and properties was performed at the Changping site of Peking University in Beijing during May–June 2016. Further information about the site and experimental details of this study are provided in Paper V.

In this study, I developed a new instrument control software program for the CPMA to regulate the cycle of particle mass measurements to allow the acquisition of measurements for six particle sizes (50, 80, 100, 150, 240, and 350 nm) in 1 hour. This automated the CPMA's operation and improved the overall experimental efficiency of the DMA-CPMA running cycle to facilitate the measurement of ambient monodisperse aerosol densities.

Figure 4.13 shows the size-resolved particle effective densities from field measurements and lab experiments. A general trend of decreasing effective density with increasing particle mobility diameter was observed in both the field measurements and lab experiments, in keeping with observations made at Riverside in the Los Angeles Basin, where vehicles were the main sources of the dominant soot aggregates in the primary atmospheric particles⁶. In the lab experiments, the effective density of pure BC was always smaller than that of the coated BC of the same size. In general, the ambient particles in the field measurements had greater effective densities (average $\sim 1.5 \text{ g cm}^{-3}$) than lab-generated coated BC particles. Since there was no apparent density peak for the BC particles observed in the field study, it may be that the ambient BC particles at the Beijing site were internally mixed with other aerosol components such as SOA, sulfate and nitrate, and heavily coated. In addition, the particle effective densities during field measurements decreased much

slower than the fresh and coated BC particles in lab experiments with increase of D_p , indicating that externally mixed secondary aerosol without BC cores may exist in each size. The comparisons discussed above (see Figure 4.13) show that the results of the lab experiments presented in this thesis can be used to interpret field measurements and clarify the mixing and transformation of BC particles in the ambient air.

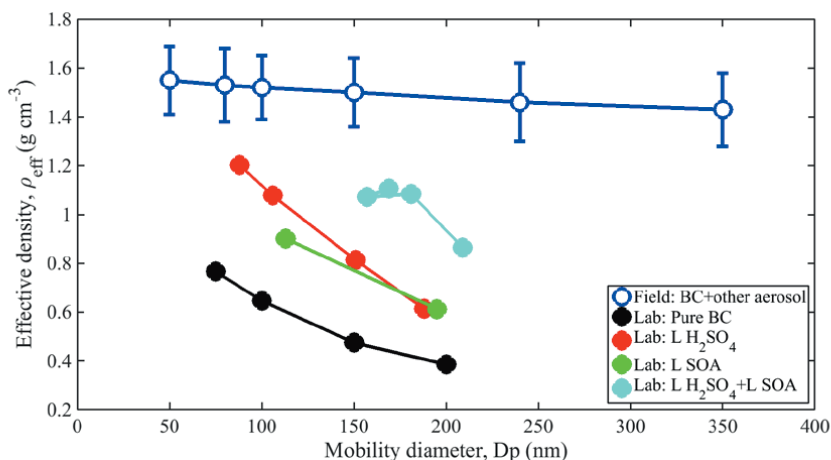


Figure 4.13 Size-resolved particle effective densities from field measurements and lab experiments. The blue circles represent the effective density of particles in ambient air averaged over the entire measurement campaign. The black, red, green and cyan dots represent pure BC, BC coated with the large level of sulfuric acid, BC coated with large level of SOA, and BC coated with the large level of sulfuric acid and the large level of SOA in the lab experiments, respectively.

Figure 4.14 shows the diurnal variation in the effective densities of 100 nm and 350 nm particles averaged over the entire campaign. The effective densities of 100 nm and 350 nm particles were higher during daytime than during nighttime. This may be because levels of sulfate, nitrate and ammonium (SNA, material density: ~ 1.8 g cm $^{-3}$) were elevated during the day (possibly as a consequence of strong photochemical reactions in the afternoon) and contributed to an increase in the effective density of BC particles. The effective density of 100 nm particles (~ 1.45 g cm $^{-3}$) was lowest between 8:00 and 9:00 in the morning due to the influence of intensive traffic emissions (outflow from the urban regions). However, that of 350 nm particles (~ 1.36 g cm $^{-3}$) was lowest around 6:00 because of biomass burning, which was observed near the sampling site in the early morning on almost every day of the measurement campaign.

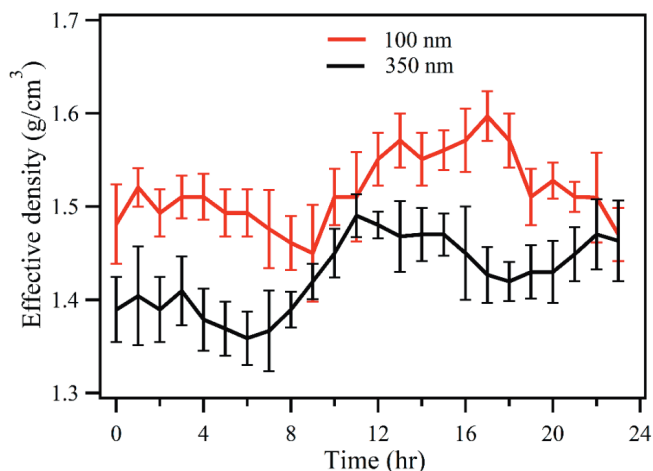


Figure 4.14 Diurnal variation in the effective densities of 100 nm and 350 nm particles averaged over the entire campaign.

Figure 4.15 shows the average effective density distributions for all six particle size classes during the nighttime period (19:00–22:00), when primary emissions were high (probably because of biomass burning). The 19:00–22:00 time period was selected to avoid the influence of aging processes caused by photochemical reactions during daytime. The effective density distributions of all particle sizes featured a single predominant peak at $\sim 1.5 \text{ g cm}^{-3}$, indicating that the particles were mostly internally mixed. In addition to this dominant peak, a small peak at less than 1.0 g cm^{-3} was observed for particles larger than 100 nm, which was attributed to freshly emitted or partially aged soot (soot-containing particles). These soot-containing particles were internally mixed and moderately coated because their effective density ($0.7\text{--}0.9 \text{ g cm}^{-3}$) was comparable to that seen for particles of similar sizes in the lab experiments (see Figure 4.13).

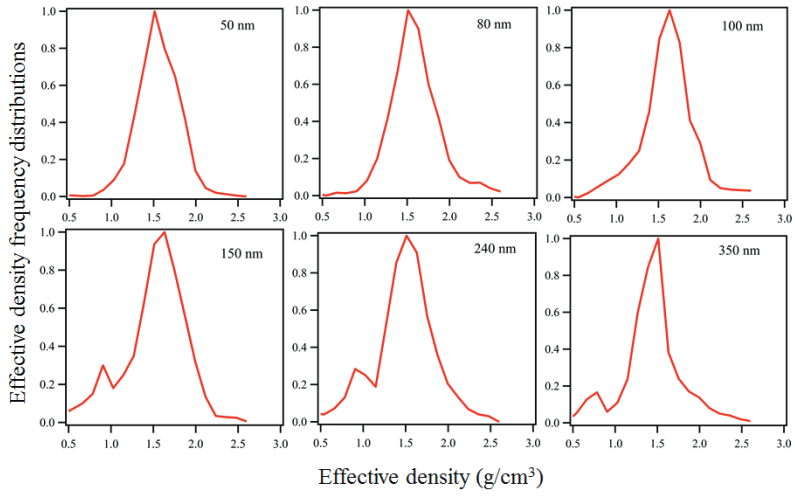


Figure 4.15 Average effective density distributions for six particle size classes during the night time (19:00–22:00).

Chapter V

Conclusions

This thesis outlines the characteristics of fresh and transformed soot observed in field and laboratory studies. The laboratory studies focused on understanding the properties of soot-containing aerosols and the interactions between soot, sulfuric acid, and secondary organic aerosol (SOA). Their findings were compared, discussed, and interpreted alongside those of the field studies. All of the studies presented herein were motivated by concerns over the impact of carbonaceous aerosols on human health, the climate, and ecosystems.

In the first study of the thesis, soot formed in an 80 kW propane-fueled industrial combustion rig was systematically characterized with respect to its size distribution, volume fraction and optical properties, i.e. absorption and scattering. The soot formed in air-rich flame primarily consisted of monomers or dimers of primary spherules at most, whereas soot from fuel-rich sooty flame consisted of aggregates of primary spherules. Absorption measurements at different locations in the flames showed that soot formed in the fuel-rich zone of the flame did not mature immediately after forming and still had organic nature, and that mature soot particles only formed after separating from the flame. The modelled radiation agreed well with the measured radiative intensities for both air-rich and fuel-rich flames. Moreover, soot absorption coefficients calculated using Rayleigh theory with complex refractive index values drawn from four different sources agreed well with the measurements.

The *in-situ* morphological characteristics of black carbon (BC) mixed with primary organic aerosol (POA) from lab-scale flame soot was studied with a new proposed framework that accounts for the evaporation of POA from soot. Using this framework, the mixing of BC and POA was linked to morphological transformation of soot particles, revealing that (i) evaporation reduced both the number and size of monodisperse particles, with the former and latter reductions being characteristic of the external and internal mixing states, respectively; (ii) the presence of externally mixed BC can be inferred from the observation of two soot peaks upon heating; and (iii) heat-induced collapse of the BC core may be caused by the evaporation of material from voids and the effects of heat. In addition, POA in BC and POA mixtures was found to be highly light-absorptive at short wavelengths: at 405 nm, the mass absorption cross section (MAC) values of POA were 2–5 m²g⁻¹, whereas those of pure BC were 8–9 m²g⁻¹.

The morphological transformation of soot aggregates induced by the condensation of vapors of sulfuric acid, and/or limonene ozonolysis products was found to result

from a two-step process involving (i) filling of voids within the aggregates, and (ii) particle mobility diameter growth. This process continued in several sequential steps until all the void space within the soot aggregate was filled. Subsequently, the growth of spherical particles proceeded for as long as vapor condensation continued. A framework was developed based on these processes to quantify the microphysical transformation of soot induced by the condensation of coating materials, i.e., the percentage of material consumed by filling and growth at each step of the transformation. The fraction of internal voids and open voids of soot can also be estimated using this framework, and this information can be used to derive a new *in-situ* dynamic shape factor that accounts for internal voids. This new framework can be applied in model development, which has significant implications for quantifying the morphological transformation of soot in the atmosphere.

The changes in optical properties of soot aggregates induced by condensation of vapors of sulfuric acid, and/or limonene ozonolysis products were also investigated. The light absorption enhancement of soot was attributed to four major processes: (i) changes in the electronic properties of the soot surface due to the chemical reaction between the soot and the condensed material; (ii) the heterogeneous chemistry between the soot surface and atmospheric oxidants such as ozone, which causes changes in electronic properties of soot; (iii) the formation of BrC in acidity-mediated SOA; and (iv) the lensing effect of the condensed material, which depends on its optical nature (refractive index). A framework for quantifying the contributions of these four processes was developed, and can be used to model the radiative forcing of BC in the atmosphere.

Finally, a field measurement at a rural site in Beijing during summertime focusing on the effective density of atmospheric aerosol particles showed that these particles had a substantial organic fraction. In most cases, a single peak with a density of $\sim 1.5 \text{ g cm}^{-3}$ was observed, indicating that soot particles were internally mixed with other aerosol components including organics, sulfate, and nitrate. The average particle density during the daytime was higher than during the nighttime, indicating that strong photochemical reactions occurred during the day, leading to the formation of secondary aerosols dominated by heavier materials such as sulfate and nitrate. At night (19:00-22:00), a small density mode with values lower than 1 g cm^{-3} was observed, which can be attributed to freshly emitted soot or partially aged soot with a thin coating.

Acknowledgements

First and foremost, I would like to express my sincere gratitude to my supervisor Docent Ravi Kant Pathak for guiding me and influencing me in many aspects during my PhD studies, for his patience, motivation, enthusiasm, and immense knowledge. I thank him for introducing me to the area of soot studies and for fruitful discussions and scientific support. My sincere thanks also go to my assistant supervisor, Prof. Mattias Hallquist, for his encouragement, insightful comments, and hard questions. I must also thank Prof. Johan Boman for being my examiner and helping me greatly during my studies.

My great appreciation also goes to Prof. Jan B.C. Pettersson, Prof. Evert Ljungström and Dr. Erik Thomson. It has been an honor to work with them. I also owe earnest and sincere thanks to all the current and former members of the Atmospheric Science group, including Anna Luts, Sofia Johansson, Julia Hammes, Ågot Watne, Magda Psichoudaki, Eva Emanuelsson, Samuel Mwaniki Gaita, Dan Gall, Dimitri Castarède, Nondas Tsiligiannis, Christian Mark Salvador, Xiangrui Kong, Michael Le Breton, Cameron Faxon, Kent Salo, Jonathan Westerlund, and Torbjörn Gustafsson. I am grateful to you all for your understanding and encouraging gestures!

All collaborators during my PhD studies are also owed many thanks for all their help and support: Maria Bech Poulsen, Erik Ahlberg, Axel C. Eriksson, Cerina Wittbom, Senior lecturer Joakim Pagels, Senior lecturer Birgitta Svenningsson, and Prof. Erik Swietlicki, etc. from Lund University; Daniel Bäckström, Maria Zetterdahl and Prof. Johan Mellqvist from Chalmers; Jana Moldanová and Åsa Hallquist from IVL.

I want to express my deep gratitude to Prof. Min Hu at Peking University who enlightened me and led me into the field of aerosol science, and Prof. Chak Chan for providing the opportunity for me to do an exchange study at HKUST.

Thanks to Song Guo, Zhijun Wu, Jianfei Peng, Yujue Wang, Jie Chen, Dongjie Shang, Hui Yun, Yuchen Wang and all the other friends, for all the fun we have had in the last years. Thanks to Qianyun Liu, Dandan Huang, Yiming Qin, Yangxi Chu, Hao Wang, etc., they made me feel at home when I was in Hong Kong!

I also want to thank my parents, for giving birth to me in the first place, supporting me spiritually throughout my life, and believing in me when I doubted myself.

Finally, I am eternally grateful to my wife Yu Jiao. Our happy marriage has been one of my proudest achievements during my PhD. I am truly thankful to my wife for encouraging me to pursue my dreams and goals, and I would like to offer this thesis as a gift to our expected child.

References

- 1 IPCC. *Climate Change 2013: The Physical Science Basis. Contribution of Working Group I to the Fifth Assessment Report of the Intergovernmental Panel on Climate Change*. (Cambridge University Press, 2013).
- 2 Nakayama, T. *et al.* Missing ozone-induced potential aerosol formation in a suburban deciduous forest. *Atmos. Environ.* **171**, 91-97 (2017).
- 3 Volkamer, R. *et al.* Secondary organic aerosol formation from anthropogenic air pollution: Rapid and higher than expected. *Geophys. Res. Lett.* **33**, L17811 (2006).
- 4 Beardsley, R. L. & Jang, M. Simulating the SOA formation of isoprene from partitioning and aerosol phase reactions in the presence of inorganics. *Atmos. Chem. Phys.* **16**, 5993-6009 (2016).
- 5 Weijers, E. P. *et al.* Anthropogenic and natural constituents in particulate matter in the Netherlands. *Atmos. Chem. Phys.* **11**, 2281-2294 (2011).
- 6 Kennedy, I. M. The health effects of combustion-generated aerosols. *Proc. Combust. Inst.* **31**, 2757-2770 (2007).
- 7 Bond, T. C. *et al.* Bounding the role of black carbon in the climate system: a scientific assessment. *J. Geophys. Res.- Atmos.* **118**, 5380-5552 (2013).
- 8 Bond, T. C. & Bergstrom, R. W. Light absorption by carbonaceous particles: an investigative review. *Aerosol Sci. Technol.* **40**, 27-67 (2006).
- 9 Kirchstetter, T. W., Novakov, T. & Hobbs, P. V. Evidence that the spectral dependence of light absorption by aerosols is affected by organic carbon. *J. Geophys. Res.- Atmos.* **109** (2004).
- 10 Schnaiter, M. *et al.* Strong spectral dependence of light absorption by organic carbon particles formed by propane combustion. *Atmos. Chem. Phys.* **6**, 2981-2990 (2006).
- 11 Wang, H. Formation of nascent soot and other condensed-phase materials in flames. *Proc. Combust. Inst.* **33**, 41-67 (2011).
- 12 D'Anna, A., Rolando, A., Allouis, C., Minutolo, P. & D'Alessio, A. Nano-organic carbon and soot particle measurements in a laminar ethylene diffusion flame. *Proc. Combust. Inst.* **30**, 1449-1456 (2005).
- 13 Frenklach, M. & Wang, H. Detailed modeling of soot particle nucleation and growth. *Symp. (Int.) Combust.* **23**, 1559-1566 (1991).
- 14 Dobbins, R. A. Soot inception temperature and the carbonization rate of precursor particles. *Combust. Flame* **130**, 204-214 (2002).
- 15 Kholghy, M. R., Veshkini, A. & Thomson, M. J. The core-shell internal nanostructure of soot – a criterion to model soot maturity. *Carbon* **100**, 508-536 (2016).
- 16 Sorensen, C. M. The mobility of fractal aggregates: a review. *Aerosol Sci. Technol.* **45**, 765-779 (2011).
- 17 Park, K., Cao, F., Kittelson, D. B. & McMurry, P. H. Relationship between particle mass and mobility for diesel exhaust particles. *Environ. Sci. Technol.* **37**, 577-583 (2003).
- 18 Maricq, M. M. & Xu, N. The effective density and fractal dimension of soot particles from premixed flames and motor vehicle exhaust. *J. Aerosol Sci.* **35**, 1251-1274 (2004).
- 19 Schnaiter, M. *et al.* UV-VIS-NIR spectral optical properties of soot and soot-containing aerosols. *J. Aerosol Sci.* **34**, 1421-1444 (2003).
- 20 Kim, J. *et al.* Assessing optical properties and refractive index of combustion aerosol particles through combined experimental and modeling studies. *Aerosol Sci. Technol.* **49**, 340-350 (2015).

- 21 Laskin, A., Laskin, J. & Nizkorodov, S. A. Chemistry of Atmospheric Brown Carbon. *Chem. Rev.* **115**, 4335-4382 (2015).
- 22 Lu, Z. *et al.* Light absorption properties and radiative effects of primary organic aerosol emissions. *Environ. Sci. Technol.* **49**, 4868-4877 (2015).
- 23 Feng, Y., Ramanathan, V. & Kotamarthi, V. R. Brown carbon: a significant atmospheric absorber of solar radiation? *Atmos. Chem. Phys.* **13**, 8607-8621 (2013).
- 24 Weingartner, E., Burtscher, H. & Baltensperger, U. Hygroscopic properties of carbon and diesel soot particles. *Atmos. Environ.* **31**, 2311-2327 (1997).
- 25 Zhang, R. *et al.* Variability in morphology, hygroscopicity, and optical properties of soot aerosols during atmospheric processing. *Proc. Natl. Acad. Sci.* **105**, 10291-10296 (2008).
- 26 Pagels, J., Khalizov, A. F., McMurry, P. H. & Zhang, R. Y. Processing of soot by controlled sulphuric acid and water condensation – mass and mobility relationship. *Aerosol Sci. Technol.* **43**, 629-640 (2009).
- 27 Schnitzler, E. G., Dutt, A., Charbonneau, A. M., Olfert, J. S. & Jäger, W. Soot aggregate restructuring due to coatings of secondary organic aerosol derived from aromatic precursors. *Environ. Sci. Technol.* **48**, 14309-14316 (2014).
- 28 Xue, H., Khalizov, A. F., Wang, L., Zheng, J. & Zhang, R. Effects of dicarboxylic acid coating on the optical properties of soot. *Phys. Chem. Chem. Phys.* **11**, 7869-7875 (2009).
- 29 Khalizov, A. F., Xue, H., Wang, L., Zheng, J. & Zhang, R. Enhanced light absorption and scattering by carbon soot aerosol internally mixed with sulfuric acid. *J. Phys. Chem. A* **113**, 1066-1074 (2009).
- 30 Shiraiwa, M., Kondo, Y., Iwamoto, T. & Kita, K. Amplification of light absorption of black carbon by organic coating. *Aerosol Sci. Technol.* **44**, 46-54 (2010).
- 31 Qiu, C., Khalizov, A. F. & Zhang, R. Soot aging from OH-initiated oxidation of toluene. *Environ. Sci. Technol.* **46**, 9464-9472 (2012).
- 32 Lambe, A. T. *et al.* Oxidative aging and cloud condensation nuclei activation of laboratory combustion soot. *J. Aerosol Sci.* **79**, 31-39 (2015).
- 33 Khalizov, A. F. *et al.* Role of OH-initiated oxidation of isoprene in aging of combustion soot. *Environ. Sci. Technol.* **47**, 2254-2263 (2013).
- 34 Weingartner, E., Baltensperger, U. & Burtscher, H. Growth and structural change of combustion aerosols at high relative humidity. *Environ. Sci. Technol.* **29**, 2982-2986 (1995).
- 35 Xue, H., Khalizov, A. F., Wang, L., Zheng, J. & Zhang, R. Effects of coating of dicarboxylic acids on the mass-mobility relationship of soot particles. *Environ. Sci. Technol.* **3**, 2787-2792 (2009).
- 36 Lewis, K. A. *et al.* Reduction in biomass burning aerosol light absorption upon humidification: roles of inorganically-induced hygroscopicity, particle collapse, and photoacoustic heat and mass transfer. *Atmos. Chem. Phys.* **9**, 8949-8966 (2009).
- 37 Fuller, K. A., Malm, W. C. & Kreidenweis, S. M. Effects of mixing on extinction by carbonaceous particles. *J. Geophys. Res.- Atmos.* **104**, 15941-15954 (1999).
- 38 Bueno, P. A. *et al.* Photoacoustic measurements of amplification of the absorption cross section for coated soot aerosols. *Aerosol Sci. Technol.* **45**, 1217-1230 (2011).
- 39 Cross, E. S. *et al.* Soot particle studies – instrument inter-comparison – project overview. *Aerosol Sci. Technol.* **44**, 592-611 (2010).
- 40 Slowik, J. G. *et al.* An inter-comparison of instruments measuring black carbon content of soot particles. *Aerosol Sci. Technol.* **41**, 295-314 (2007).
- 41 Guo, S. *et al.* OH-initiated oxidation of m-xylene on black carbon aging. *Environ. Sci. Technol.* **50**, 8605-8612 (2016).

- 42 Knox, A. *et al.* Mass absorption cross-section of ambient black carbon aerosol in
relation to chemical age. *Aerosol Sci. Technol.* **43**, 522-532 (2009).
- 43 Lack, D. A. *et al.* Brown carbon and internal mixing in biomass burning particles.
Proc. Natl. Acad. Sci. **109**, 14802-14807 (2012).
- 44 Liu, S. *et al.* Enhanced light absorption by mixed source black and brown carbon
particles in UK winter. *Nat. Commun.* **6**, 8435 (2015).
- 45 Cui, X. *et al.* Radiative absorption enhancement from coatings on black carbon
aerosols. *Sci. Total Environ.* **551-552**, 51-56 (2016).
- 46 Cappa, C. D. *et al.* Radiative absorption enhancements due to the mixing state of
atmospheric black carbon. *Science* **337**, 1078-1081 (2012).
- 47 Healy, R. M. *et al.* Light-absorbing properties of ambient black carbon and brown
carbon from fossil fuel and biomass burning sources. *J. Geophys. Res.- Atmos.* **120**,
6619-6633 (2015).
- 48 Peng, J. *et al.* Markedly enhanced absorption and direct radiative forcing of black
carbon under polluted urban environments. *Proc. Natl. Acad. Sci.* **113**, 4266-4271
(2016).
- 49 Mikhailov, E. F., Vlasenko, S. S., Podgorny, I. A., Ramanathan, V. & Corrigan, C. E.
Optical properties of soot-water drop agglomerates: an experimental study. *J.*
Geophys. Res.- Atmos. **111**, D07209 (2006).
- 50 Tritscher, T. *et al.* Changes of hygroscopicity and morphology during ageing of diesel
soot. *Environ. Res. Lett.* **6**, 034026 (2011).
- 51 Wang, J., Cubison, M. J., Aiken, A. C., Jimenez, J. L. & Collins, D. R. The
importance of aerosol mixing state and size-resolved composition on CCN
concentration and the variation of the importance with atmospheric aging of aerosols.
Atmos. Chem. Phys. **10**, 7267-7283 (2010).
- 52 Hings, S. S. *et al.* CCN activation experiments with adipic acid: effect of particle
phase and adipic acid coatings on soluble and insoluble particles. *Atmos. Chem. Phys.*
8, 3735-3748 (2008).
- 53 Henning, S. *et al.* Hygroscopic growth and droplet activation of soot particles:
uncoated, succinic or sulfuric acid coated. *Atmos. Chem. Phys.* **12**, 4525-4537 (2012).
- 54 Wittbom, C. *et al.* Cloud droplet activity changes of soot aerosol upon smog chamber
ageing. *Atmos. Chem. Phys.* **14**, 9831-9854 (2014).
- 55 Koch, D. & Del Genio, A. D. Black carbon semi-direct effects on cloud cover: review
and synthesis. *Atmos. Chem. Phys.* **10**, 7685-7696 (2010).
- 56 Ban-Weiss, G., Cao, L., Bala, G. & Caldeira, K. Dependence of climate forcing and
response on the altitude of black carbon aerosols. *Clim. Dyn.* **38**, 897-911 (2012).
- 57 Takemura, T. & Uchida, T. Global climate modeling of regional changes in cloud,
precipitation, and radiation budget due to the aerosol semi-direct effect of black
carbon. *SOLA* **7**, 181-184 (2011).
- 58 Janssen, N. A. *et al.* Black carbon as an additional indicator of the adverse health
effects of airborne particles compared with PM₁₀ and PM_{2.5}. *Environ. Health Perspect.*
119, 1691-1699 (2011).
- 59 Wierzbicka, A. *et al.* Detailed diesel exhaust characteristics including particle surface
area and lung deposited dose for better understanding of health effects in human
chamber exposure studies. *Atmos. Environ.* **86**, 212-219 (2014).
- 60 Ristovski, Z. D. *et al.* Respiratory health effects of diesel particulate matter.
Respirology **17**, 201-212 (2012).
- 61 Khalizov, A. F. *et al.* Formation of highly hygroscopic soot aerosols upon internal
mixing with sulfuric acid vapor. *J. Geophys. Res.- Atmos.* **114**, D05208 (2009).

- 62 Hjærtstam, S., Johansson, R., Andersson, K. & Johnsson, F. Computational fluid dynamics modeling of oxy-fuel flames: the role of soot and gas radiation. *Energy Fuels* **26**, 2786-2797 (2012).
- 63 Jing, L. Standard combustion aerosol generator (SCAG) for calibration purposes. *3rd ETH workshop on nanoparticle measurement CD-ROM* (1999).
- 64 Huffman, J. A., Ziemann, P. J., Jayne, J. T., Worsnop, D. R. & Jimenez, J. L. Development and characterization of a fast-stepping/scanning thermodenuder for chemically-resolved aerosol volatility measurements. *Aerosol Sci. Technol.* **42**, 395-407 (2008).
- 65 Burtscher, H. *et al.* Separation of volatile and non-volatile aerosol fractions by thermodesorption: instrumental development and applications. *J. Aerosol Sci.* **32**, 427-442 (2001).
- 66 Jonsson, Å. M., Hallquist, M. & Ljungström, E. The effect of temperature and water on secondary organic aerosol formation from ozonolysis of limonene, Δ^3 -carene and α -pinene. *Atmos. Chem. Phys.* **8**, 6541-6549 (2008).
- 67 Rissler, J. *et al.* Effective density characterization of soot agglomerates from various sources and comparison to aggregation theory. *Aerosol Sci. Technol.* **47**, 792-805 (2013).
- 68 CPMA User Manual. (Cambustion Limited Co., Version 1.53, 2011).
- 69 McMurry, P. H., Wang, X., Park, K. & Ehara, K. The relationship between mass and mobility for atmospheric particles: a new technique for measuring particle density. *Aerosol Sci. Technol.* **36**, 227-238 (2002).
- 70 Olfert, J. S. & Collings, N. New method for particle mass classification – the Couette centrifugal particle mass analyzer. *J. Aerosol Sci.* **36**, 1338-1352 (2005).
- 71 Arnott, W. P., Moosmüller, H., Fred Rogers, C., Jin, T. & Bruch, R. Photoacoustic spectrometer for measuring light absorption by aerosol: instrument description. *Atmos. Environ.* **33**, 2845-2852 (1999).
- 72 Andersson, K., Johansson, R., Johnsson, F. & Leckner, B. Radiation intensity of propane-fired oxy-fuel flames: implications for soot formation. *Energy Fuels* **22**, 1535-1541 (2008).
- 73 Lighty, J. S., Veranth, J. M. & Sarofim, A. F. Combustion aerosols: factors governing their size and composition and implications to human health. *J. Air Waste Manag. Assoc.* **50**, 1565-1618 (2000).
- 74 Modest, M. F. in *Radiative Heat Transfer* Ch. II, 361-412 (Academic Press, Burlington, 2003).
- 75 Stull, V. R. & Plass, G. N. Emissivity of dispersed carbon particles. *J. Opt. Soc. Am.* **50**, 121-129 (1960).
- 76 Dalzell, W. H. & Sarofim, A. F. Optical constants of soot and their application to heat-flux calculations. *J. Heat Transfer* **91**, 100-104 (1969).
- 77 Lee, S. C. & Tien, C. L. Optical constants of soot in hydrocarbon flames. *Symp. (Int.) Combust.* **18**, 1159-1166 (1981).
- 78 Chang, H. & Charalampopoulos, T. T. Determination of the wavelength dependence of refractive indices of flame soot. *Proc. Royal Soc. A* **430**, 577-591 (1990).
- 79 Johansson, R., Leckner, B., Andersson, K. & Johnsson, F. Influence of particle and gas radiation in oxy-fuel combustion. *Int. J. Heat Mass Transfer* **65**, 143-152 (2013).
- 80 Malkmus, W. Random Lorentz band model with exponential-tailed S-1 line-intensity distribution function. *J. Opt. Soc. Am.* **57**, 323-329 (1967).
- 81 Moore, R. H. *et al.* Mapping the operation of the miniature combustion aerosol standard (mini-CAST) soot generator. *Aerosol Sci. Technol.* **48**, 467-479 (2014).

- 82 Dickau, M. *et al.* Methodology for quantifying the volatile mixing state of an aerosol. *Aerosol Sci. Technol.* **50**, 759-772 (2016).
- 83 Sgro, L. A. *et al.* Measurements of nanoparticles of organic carbon and soot in flames and vehicle exhausts. *Environ. Sci. Technol.* **42**, 859-863 (2008).
- 84 Maricq, M. M. Examining the relationship between black carbon and soot in flames and engine exhaust. *Aerosol Sci. Technol.* **48**, 620-629 (2014).
- 85 Andreae, M. O. & Gelencsér, A. Black carbon or brown carbon? The nature of light-absorbing carbonaceous aerosols. *Atmos. Chem. Phys.* **6**, 3131-3148 (2006).
- 86 Hennig, G. The properties of the interstitial compounds of graphite. I. the electronic structure of graphite bisulfate. *J. Chem. Phys.* **19**, 922-929 (1951).
- 87 Kmetko, E. A. Electronic properties of carbons and of their interstitial bisulfate compounds. *J. Chem. Phys.* **21**, 2152-2158 (1953).
- 88 Zhang, D. & Zhang, R. Laboratory investigation of heterogeneous interaction of sulfuric acid with soot. *Environ. Sci. Technol.* **39**, 5722-5728 (2005).
- 89 Rai, P. K., Parra-Vasquez, A. N. G., Peng, H., Hauge, R. H. & Pasquali, M. Solubility and size separation of large fullerenes in concentrated sulfuric acids. *J. Phys. Chem. C* **111**, 17966-17969 (2007).
- 90 Kovtyukhova, N. I. *et al.* Non-oxidative intercalation and exfoliation of graphite by Brønsted acids. *Nat. Chem.* **6**, 957-963 (2014).
- 91 Kim, H. & Paulson, S. E. Real refractive indices and volatility of secondary organic aerosol generated from photooxidation and ozonolysis of limonene, α -pinene and toluene. *Atmos. Chem. Phys.* **13**, 7711-7723 (2013).
- 92 Kim, H., Barkey, B. & Paulson, S. E. Real refractive indices and formation yields of secondary organic aerosol generated from photooxidation of limonene and α -pinene: the effect of the HC/NO_x ratio. *J. Phys. Chem. A* **116**, 6059-6067 (2012).
- 93 Smith, D. M. & Chughtai, A. R. Reaction kinetics of ozone at low concentrations with n-hexane soot. *J. Geophys. Res.- Atmos.* **101**, 19607-19620 (1996).
- 94 Cataldo, F. Ozone reaction with carbon nanostructures 2: the reaction of ozone with milled graphite and different carbon black grades. *J. Nanosci. Nanotechnol.* **7**, 1446-1454 (2007).
- 95 Streitwieser, A., Heathcock, C. H. & Kosower, E. M. *Introduction to organic chemistry.* (Maxwell Macmillan International, 1992).
- 96 Geller, M., Biswas, S. & Sioutas, C. Determination of particle effective density in urban environments with a differential mobility analyzer and aerosol particle mass analyzer. *Aerosol Sci. Technol.* **40**, 709-723 (2006).

